Detecting Milky Way stellar streams in gravitational waves

THESIS

submitted in partial fulfillment of the
requirements for the degree of

MASTER OF SCIENCE
in
PHYSICS

Author :	Saeid Mahmoudzadeh
Student ID :	s2547341
Supervisor :	Dr. Elena Maria Rossi
Co-supervisor :	Dr. Valeriya Korol
Second reader :	Dr. Marius Cauntun

Leiden, The Netherlands, August 18, 2021

Detecting Milky Way stellar streams in gravitational waves

Saeid Mahmoudzadeh

Instituut-Lorentz, Leiden University
P.O. Box 9500, 2300 RA Leiden, The Netherlands

August 18, 2021

Abstract

The Milky Way halo embeds several satellites galaxies that carry information about the structure formation history of our Galaxy. Some of these satellites are disrupted by the galactic tidal forces and form the stellar streams, which typically have a lower mass compared to their progenitor. The Laser Interferometer Space Antenna (LISA) can detect these structures in gravitational wave emission, allowing us to study their properties. The most numerous gravitational sources in the Galactic halo are the population of white dwarf (WD) binaries. In this work, we combine a cosmological simulation of the Milky Way halo with a binary population synthesis model to find the realistic distribution of WD binary systems. We study the properties of the detectable binary systems in the Galactic halo and constrain the total stellar mass, distance, and age of its satellites and streams. A spectacular example of a disrupted satellite is Sagittarius. Its stream extends all across the sky, and due to its large stellar mass and close distance, it is expected to host several LISA detections. We provide the first estimation of the Sagittarius WD binary population using a similar approach employing positions and densities from a Sagittaruis simulation and inferred age distribution from observation. We predict that LISA will detect ~ 30 binaries, from which 10 will be in the Sagittarius stream.

Contents

Chapter 1

Introduction

1.1 Gravitational wave astronomy

Einstein proposed the theory of general relativity (GR) (Einstein, 1915). According to this theory, the geometry of spacetime, as characterized by curvature, is determined by the existence of matter and energy. Under certain conditions, accelerating massive objects can disturb the curvature. Einstein anticipated gravitational waves (GWs) as the perturbations in spacetime curvature that propagate at the speed of light (Einstein, 1916). He later demonstrated that when a system emits GWs, it must also emit energy, which reacts by dampening the motions in the system (Einstein & Rosen, 1937).

When GWs pass through an observer, the observer's frame deforms according to the strain of the GWs. The strain of GWs is intrinsically very small ($\sim 10^{-22}$, see also Section 5.3) and decreases by distance from the source. Because of the long distance to GW sources, their effects on Earth are predicted to be quite small, making them hard to detect. Sources of noise, on the other hand, may also dominate the signal. As a result, there are two methods for detecting these waves: creating highly sensitive instruments or measuring energy loss over a lengthy period of time. Many attempts have been made to detect GWs since the existence of GWs was proposed. Hulse & Taylor (1975) made the first indirect observation of GWs as they discovered a binary system consists of a neutron star and a pulsar PSR1913+16 whose orbit decays in agreement with the energy loss due to GWs emission . However, GWs had not been directly detected until 2015 by the Laser Interferometer Gravitational-Wave Observatory (LIGO) Abbott et al. (2016b). The existence of such waves was demonstrated by the observation of the merger event GW150914 of a pair of black holes

with masses of about 36 and 29 solar masses. This discovery established a new era of gravitational-wave astronomy, allowing for the observation of dynamical strong-field gravity and providing a direct probe for testing the validity of GR in the nonlinear range. Furthermore, if GR holds across all ranges, we can look for unexpected local matter and new exotic fields that may exist near black holes. GWs may also be able to provide us with firsthand observation of the very early moments of the Universe (Amaro-Seoane et al., 2017a). Later in 2017, GW170817, the first merger of binary neutron stars was discovered from gravitational wave and electromagnetic (EM) radiation. Combining the gravitational-wave data with the observations of emissions enables us to gain new insights into the astrophysics of compact binary systems, gamma-ray bursts, and independent cosmological tests (Abbott et al., 2017).

The ground-based interferometer LIGO is composed of two 4 km long arms in an L-shape. It splits a beam directed from a laser source into these two arms. Splitted waves are reflected back to the beam splitter, where they are combined and directed to the detector. If both beams travel equal distances, the combined beam destructively interferes. Therefore, there will be no pattern signal. However, when the GW passes through, it changes the distance between the mirrors, resulting in a phase shift between the light beams that LIGO receives at the detector and produces. This phase shift is the physical observable that indicates the presence of a GW. Laser Interferometer GW detectors look for temporal variations in time series data rather than spatial variations caused by a passing GW (Maggiore, 2007). As a result, LIGO can detect GWs that are substantially smaller than the detector size. The Earth is constantly moving, causing the mirrors in the detectors to shake at a frequency ranging from 1 to 10 Hz. This, combined with Seismic noise, precludes ground-based interferometers from searching for GWs at frequencies lower than around 10 Hz. Consequently, the frequency range of LIGO sensitivity is 10 Hz to 10 kHz (Abbott et al., 2016a).

1.1.1 Laser Interferometer Space Antenna

To overcome the low frequency sensitivity limit set by seismic noise on Earth, space-based GW experiments have been proposed (Folkner et al., 1998). For example, the Laser Interferometer Space Antenna (LISA) comprises three spacecraft separated by 2.5 million kilometers that form an equilateral triangle following Earth in its orbit around the Sun at a dis-

tance of 50 million kilometers from Earth and is scheduled for launch in 2034. As planned in the L3 mission, LISA will provide observation over a science lifetime of at least four years. The frequency range of LISA sensitivity is 10^{-4} Hz to 1 Hz. Hence, it will be able to detect objects with longer wavelengths in GWs corresponding to wider orbits and perhaps considerably heavier than those detected by LIGO (Amaro-Seoane et al., 2017b). LISA is predicted to be able to pinpoint the position of GW sources to ten squared degree or less – this is in favorable conditions – due to the orbital motion of the detector and, to a lesser extent, the inherent directionality of the detectors (Amaro-Seoane et al., 2017a).

1.1.2 GW Sources

In general, LISA GW sources can be categorized into (Hughes, 2006):

- **Stochastic sources from cosmological backgrounds**: They consist of a superposition of various, uncorrelated sources, the majority of which are cosmological in origin and have been amplified by inflation. They feature a broad, flat, or widely peaked spectrum, and their frequency can range from 10^{-16} to 10^{10} Hz.

- **Periodic sources, Galactic binary stars**: They are guaranteed sources of GWs as we measure their GW radiation indirectly with telescopes (see the example of PSR1913+16 above) which are in binary systems (mostly WD binaries) that radiate at nearly a pure tone (monochromatic) in their rest frame.

- **Chirping sources, Massive black hole coalescence**: Binaries with a total mass of $10^4 - 10^7 M_\odot$ formed by the merging of large structures – galaxies and protogalaxies – and the dark matter halos that host them, emitting a pure tone that swiftly passes through the LISA band.

- **Complicated chirping sources, Extreme mass ratio inspirals**: They consist of a binary system, one of which is a massive Galactic core black hole and the other a stellar mass compact object.

Version of August 18, 2021– Created August 18, 2021 - 10:17

1.2 Probing our Galaxy with gravitational wave sources in LISA

Our galaxy, the Milky Way (MW), is expected to host a large number of stellar binaries (composed of WD, neutron star (NS), and black hole (BH) in short-period orbits of < 1 hour) emitting GWs (Nelemans et al., 2001b). We can use LISA as a tool for studying our Galaxy through GW radiation from these binaries. The MW can be divided into visible components: a thin disk, a thick disk, a bulge, and a stellar halo, each with its own spatial and kinematic distribution, as well as age and chemical composition. The stellar halo is the most extended stellar component that contains very metal-poor and old stars (e.g. Helmi, 2020). According to the hierarchical structure formation hypothesis, galaxies like the MW have formed via a series of accretion events (e.g. Bullock & Johnston, 2005). This implies that the stellar halo should also be formed from disrupted accreted systems (Purcell et al., 2010; Zolotov et al., 2009).

1.2.1 Stellar streams

Numerical simulations suggest that stars of an infalling satellite become unbound and orbit around the parent galaxy, spreading across configuration space, i.e. phase mix. Once the debris has filled the configuration-space volume, it is considered to be fully phase-mixed. However, according to Liouville's theorem, the phase-space density of debris is conserved as it evolves, establishing a link between kinematics and the progenitor mass (Johnston, 2016). Tidal disruption of low mass progenitors (globular clusters or dwarf galaxies) with low eccentric orbits forms stellar streams that are kinematically cold and thin. The study of stellar streams in the Galactic halo gives us the opportunity to probe the MW formation history and its gravitational field (Ibata et al., 2002; Johnston et al., 1999), as well as studying the nature of dark matter (Helmi, 2020).

Gaia and other EM surveys give us astrometric and photometric measurements for various regions of the sky. There are typically three different methods applied to these data for detecting and characterizing the stellar streams. One method uses matched filter techniques on color-magnitude diagrams to identify a specific population of stars (e.g. Dehnen et al., 2004). This technique performs poorly on structures with substantial distance gradients. Another is to trace groups of stars such as RR Lyrae stars that are confined in a small phase-space volume (e.g. Duffau et al., 2006). This method needs complete kinematic information of the stars, which is not

Version of August 18, 2021– Created August 18, 2021 - 10:17

fully provided by existing measurements. More recently, Malhan & Ibata (2018) presented the STREAMFINDER algorithm, which more efficiently detects stellar streams by tracking the orbit of their stars within a Galactic potential. Figure 1.1 shows a number of stellar streams detected by STREAMFINDER within 30 kpc distance. All of the above methods are limited by foreground contamination stars and observational errors.

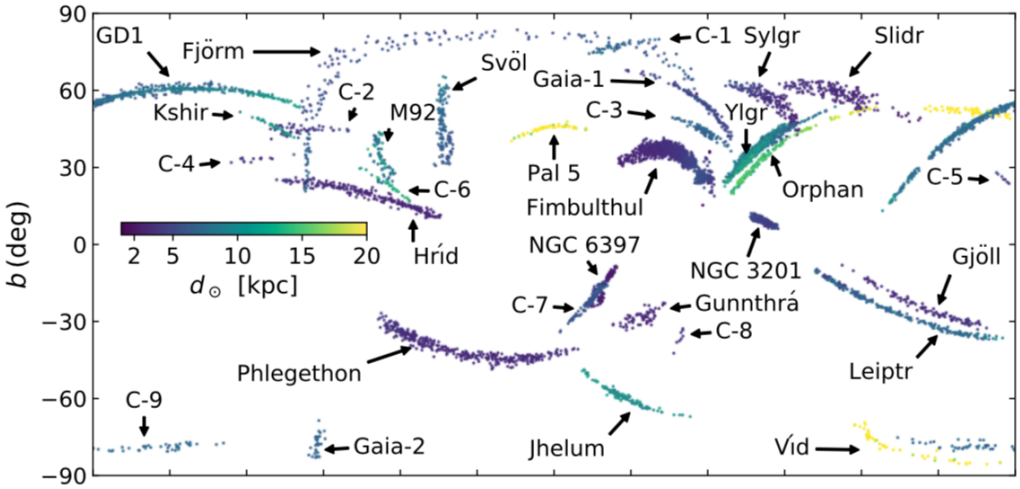

Figure 1.1: *The heliocentric distance solutions for 5960 stars from the Gaia DR2 catalog provided by* STREAMFINDER *software taken from Ibata et al. (2021), Figure 2.*

Simulations of galaxy formation estimate that the stellar halo of the MW contains 300-500 satellites at present (Moore et al., 1999). However, only 60 satellites of the same size have been observed so far (Koposov et al., 2018; Newton et al., 2018). The one order of magnitude discrepancy between the number of observed and estimated satellites could be explained by the fact that only a tiny portion of stars in stellar halos can be observed in EM waves, which are also dispersed over a large volume. This makes it challenging to study the stellar halo substructures and their global properties. However, GW astronomy can help us in overcoming this limitation.

1.2.2 Double white dwarf binaries

From GW sources, double white dwarf (DWD) binaries, which may be discovered at all galactocentric distances and span a wide range of ages, can be employed as tracers of the properties of the MW and its substructures. They can also be studied to constrain the outcome of the common

envelope phase and the progenitors of type Ia supernovae, as well as to obtain a better knowledge of WDs, their masses, and their interactions in binaries (Amaro-Seoane et al., 2013). The detectability of DWDs in the MW has been extensively studied, and LISA is estimated to detect from a few to several 10^4 DWDs. (Korol et al., 2017; Lamberts et al., 2019; Nelemans et al., 2001a; Ruiter et al., 2010). Korol et al. (2018) and later Roeber et al. (2020) demonstrated that LISA would be able to detect DWDs in our galaxy's satellites and the Local Group. When compared to black hole (Sesana et al., 2020) and neutron star (Lau et al., 2020) binaries, DWD sources in the LISA band are roughly three orders of magnitude more numerous in the MW. According to population synthesis studies, there will be so many binaries at sufficiently low frequencies (below 3 mHz) that they will be indistinguishable and form a contaminated foreground (Evans et al., 1987; Hils et al., 1990). However, frequency bins will be devoid of Galactic binaries at higher frequencies and allow to obtain information about signals from weaker extragalactic sources. This noise contains information about the distribution of stars (Hughes, 2006) and the structural properties of our galaxy (Benacquista & Holley-Bockelmann, 2006).

DWDs are classified as detached and semi-detached binary systems, the latter of which involves mass transfer beyond the Roche Lobe and therefore may be observable in X-ray (Nelemans et al., 2001b). It is generally difficult to detect DWDs at optical wavelength because they are faint and rapidly cooling down and because the dust contamination inhibits them. (Korol et al., 2019), on the other hand, we already know 25 DWDs detectable that can be detected by LISA. These binaries are referred to as "verification binaries."

1.2.3 Sagittarius

Sagittarius dwarf galaxy (Sgr) is one of the MW's closest and most massive satellites originally discovered by Ibata et al. (1994). Due to its proximity and large mass, the Sgr is expected to host several LISA detectable binaries. The ongoing tidal disruption of Sgr has resulted in a magnificent stellar stream wrapping around the MW, which may be used as a model to study the hierarchical structure formation as well as constraining the MW potential (e.g. Law & Majewski, 2010). Majewski et al. (2003) revealed the two arms of the stream, the leading in the Northern Galactic hemisphere and the trailing in the Southern Galactic hemisphere, by exploiting the prominent population of M giant stars from the Two Micron All-Sky Sur-

Version of August 18, 2021– Created August 18, 2021 - 10:17

vey (2MASS). Observational surveys such as Gaia have provided us with a detailed map of the Sgr satellite using stellar tracers, specifically RR Lyrae stars, to quantify its properties and structural characteristics such as stellar mass, distance (Hamanowicz et al., 2016), metallicity (Cseresnjes et al., 2000), and the 50 kpc difference between the apocentric distances of the leading and trailing arms (Belokurov et al., 2014). The progenitor of Sgr is located behind the Galactic bulge at a distance of $\sim$ 26.7 kpc and has Galactic coordinates $\ell = 275^\circ$ and $b = -14^\circ$ (Belokurov et al., 2014). Since its discovery, there has been a debate about the mass of the Sgr at present and initially before being disrupted by the MW. According to simulations of the disruption of Sgr, it is estimated that Sgr started merging with the MW around 10 Gyr ago with a relatively large total (stellar + dark matter) mass of $M = 10^{11} M_\odot$ (Gibbons et al., 2017; Jiang & Binney, 2000), indicating that it is not a minor merger. Law & Majewski (2010) estimated a mass of $2.5^{+1.3}_{-1.0} \times 10^8 M_\odot$ for the remnant by comparing the resulting velocity dispersion in the stream from a series of N-body simulations to its actual observed value in the trailing arm. Another estimation is provided by Vasiliev & Belokurov (2020), comparing the magnitude distribution of the observed stars with a number of well-known globular clusters of similar metallicity. They infer a total mass of around $2 \times 10^8 M_\odot$ for Sgr.

This work is organized as follows. In Chapter 2, we provide a review of the generation and detection of GWs from DWD binaries. In Chapter 3, we study the population of DWDs, the Galactic halo of the MW, using a binary population synthesis model combined with a cosmological hydrodynamic simulation of a MW-like galaxy. We identify detectable DWDs by LISA and try to constrain the properties of the satellites and their detectable binaries. We then narrow our focus to Sgr to make predictions for its detectability in LISA. Our results are presented in Chapter 4. We discuss them and provide a summary of our findings in Chapter 5.

Version of August 18, 2021– Created August 18, 2021 - 10:17

Chapter 2

Review of gravitational waves generation and detection

At this section we will review the mathematical description of the binary emission in GWs mainly based on Maggiore (2007) book, and Tong (2019) lecture notes. We begin by introducing linearized gravity in the context of the weak field approximation in a flat background. We determine the equations of motion for the metric perturbation and demonstrate that it has a plane wave solution with two polarizations. We then identify the characteristics of GWs emitted by a binary system of WDs by using some approximation.

2.1 Linearized gravity

Einstein developed theory of general relativity to generalize special relativity and refine Newton's law of gravity. At the core of the theory of general relativity, Einstein's field equations governs how the geometry of spacetime responds to energy and momentum.

$$R_{\mu\nu} - \frac{1}{2} g_{\mu\nu} R = \frac{8\pi G}{c^4} T_{\mu\nu}, \tag{2.1}$$

where $g_{\mu\nu}$ is the metric. R and $R_{\mu\nu}$ are the corresponding Ricci scalar and Ricci tensor. G is the Newton constant, c is the speed of light, and $T_{\mu\nu}$ is the energy-momentum tensor of matter. The Ricci scalar R is defined by $R = g^{\mu\nu} R_{\mu\nu}$, where the Ricci tensor $R_{\mu\nu}$ is

$$R_{\mu\nu} = \partial_\lambda \Gamma^\lambda_{\mu\nu} - \partial_\mu \Gamma^\lambda_{\lambda\nu} + \Gamma^\lambda_{\mu\nu} \Gamma^\rho_{\rho\lambda} - \Gamma^\lambda_{\nu\rho} \Gamma^\rho_{\mu\lambda}. \tag{2.2}$$

We will consider the torsion-less metric formalism ,$\partial_\lambda g_{\mu\nu} = 0$, which implies that the connections $\Gamma^\alpha_{\beta\gamma}$ can be expressed in terms of the metric tensor $g_{\mu\nu}$, as

$$\Gamma^\alpha_{\beta\gamma} = \frac{1}{2} g^{\alpha\lambda} \left(\partial_\beta g_{\gamma\lambda} + \partial_\gamma g_{\lambda\beta} - \partial_\lambda g_{\beta\gamma} \right). \tag{2.3}$$

The linearized theory assumes that the field is weak and that it varies with time. As a result, the metric can be decomposed into a flat background and a perturbation which we will see it describes the GW.

$$g_{\mu\nu} = \eta_{\mu\nu} + h_{\mu\nu}, \quad \left| h_{\mu\nu} \right| \ll 1. \tag{2.4}$$

Here $\eta_{\mu\nu} = \text{diag}(-1, +1, +1, +1)$. We expand the field equations (2.1) to the first order in terms of $h_{\mu\nu}$. Equation (2.4) does not specify the coordinate system on spacetime. In fact considering coordinate transformation from x^μ to $x^\mu + \xi^\mu$, $h_{\mu\nu}$ tansforms to $h_{\mu\nu} - 2\partial_{(\mu}\xi_{\nu)}$. Thus, slowly varying diffeomorphisms ($\left|\partial_\mu \xi_\nu\right| \ll 1$) keeps the metric perturbation small and hence is a gauge transformation in linearized theory. We will later fix this gauge to simplify our field equations.
By ignoring higher order of $h_{\mu\nu}$, we obtain the inverse metric

$$g^{\mu\nu} = \eta^{\mu\nu} - h^{\mu\nu}, \tag{2.5}$$

where $h^{\mu\nu} = \eta^{\alpha\mu}\eta^{\beta\mu}h_{\alpha\beta}$. We can then expand the Christoffel symbols

$$\Gamma^\rho_{\mu\nu} = \frac{1}{2} \eta^{\rho\lambda} \left(\partial_\mu h_{\nu\lambda} + \partial_\nu h_{\lambda\mu} - \partial_\lambda h_{\mu\nu} \right). \tag{2.6}$$

The Riemann tensor can be written in terms of Christoffel symbols

$$R_{\mu\nu}{}^\rho{}_\sigma = \partial_\mu \Gamma^\rho_{\nu\sigma} - \partial_\nu \Gamma^\rho_{\mu\sigma} + \Gamma^\rho_{\mu\lambda}\Gamma^\lambda_{\nu\sigma} - \Gamma^\rho_{\nu\lambda}\Gamma^\lambda_{\mu\sigma}. \tag{2.7}$$

Since the Christoffel symbols are at leading order in the metric perturbation h, we can neglect Γ^2 terms.

$$R_{\mu\nu}{}^\rho{}_\sigma = \partial_\mu \Gamma^\rho_{\nu\sigma} - \partial_\nu \Gamma^\rho_{\mu\sigma} = \frac{1}{2} \eta^{\rho\lambda} \left(\partial_\mu \partial_\sigma h_{\nu\lambda} - \partial_\mu \partial_\lambda h_{\nu\sigma} - \partial_\nu \partial_\sigma h_{\mu\lambda} + \partial_\nu \partial_\lambda h_{\mu\sigma} \right). \tag{2.8}$$

Contracting over μ and ρ, we obtain the Ricci tensor

$$R_{\mu\nu}{}^\mu{}_\sigma = R_{\sigma\nu} = \frac{1}{2} \left(\partial^\mu \partial_\sigma h_{\nu\mu} - \Box h_{\nu\sigma} - \partial_\nu \partial_\sigma h + \partial_\nu \partial^\mu h_{\mu\sigma} \right). \tag{2.9}$$

Version of August 18, 2021– Created August 18, 2021 - 10:17

Where $h = \eta^{\mu\nu}h_{\mu\nu}$ is the trace of perturbation and $\Box = (-1/c^2)\partial_0^2 + \partial_i^2$ is the d'Alambertian in the flat space. Renaming the indices we obtain Ricci tensor $R_{\mu\nu}$ and Ricci Scalar as

$$\begin{aligned} R_{\mu\nu} &= \frac{1}{2}\left(\partial_\mu\partial^\sigma h_{\nu\sigma} + \partial_\nu\partial^\sigma h_{\mu\sigma} - \Box h_{\mu\nu} - \partial_\mu\partial_\nu h\right), \\ R &= \eta^{\mu\nu}R_{\mu\nu} = \partial^\mu\partial^\nu h_{\mu\nu} - \Box h. \end{aligned} \tag{2.10}$$

To linear order in h, lhs of the Einstein's equation become

$$R_{\mu\nu} - \frac{1}{2}\eta_{\mu\nu}R = \frac{1}{2}\left(\partial_\mu\partial^\sigma h_{\nu\sigma} + \partial_\nu\partial^\sigma h_{\mu\sigma} - \Box h_{\mu\nu} - \partial_\mu\partial_\nu h - \eta_{\mu\nu}\partial^\rho\partial^\sigma h_{\rho\sigma} + \eta_{\mu\nu}\Box h\right) \tag{2.11}$$

We can express the above more convinently by introducing the trace-reversed metric perturbation, $\bar{h}_{\mu\nu} = h_{\mu\nu} - 1/2 b_{\mu\nu}h$, which transforms as follows

$$\begin{aligned} \bar{h}_{\mu\nu} &\to \bar{h}_{\mu\nu} - \left(\partial_\mu\xi_\nu + \partial_\nu\xi_\mu + \eta_{\mu\nu}\partial_\rho\xi^\rho\right), \\ \partial^\nu\bar{h}_{\mu\nu} &\to \partial^\nu\bar{h}_{\mu\nu} - \Box\xi_\mu. \end{aligned} \tag{2.12}$$

Rewriting the fields equation in terms of the trace-reversed metric perturbation, we obtain

$$\Box\bar{h}_{\mu\nu} + \eta_{\mu\nu}\partial^\rho\partial^\sigma\bar{h}_{\rho\sigma} - \partial_\mu\partial^\sigma\bar{h}_{\nu\sigma} - \partial_\nu\partial^\sigma\bar{h}_{\mu\sigma} = -\frac{16\pi G}{c^4}T_{\mu\nu}. \tag{2.13}$$

One can easily check that the Bianchi identity in the linearized theory is satisfied and results in the conservation of energy-momentum

$$\partial^\mu\left(R_{\mu\nu} - \frac{1}{2}\eta_{\mu\nu}R\right) = \partial^\mu T_{\mu\nu} = 0. \tag{2.14}$$

Equation (2.13) can further simplified by fixing the gauge freedom. We choose Lorenz gauge,

$$\partial^\nu\bar{h}_{\mu\nu} = 0, \tag{2.15}$$

which reduces the field equation to the linear inhomogeneous wave equation

$$\Box\bar{h}_{\mu\nu} = -\frac{16\pi G}{c^4}T_{\mu\nu}. \tag{2.16}$$

For any solution $\bar{h}_{\mu\nu}$ of the field, a gauge transformation can cancel its divergence.

$$\partial^\nu\bar{h}_{\mu\nu} \to \partial^\nu\bar{h}_{\mu\nu} - \Box\xi_\mu = 0. \tag{2.17}$$

So we can always impose the Lorenz gauge. Outside the source, where $T_{\mu\nu} = 0$, equation (2.16) becomes

$$\Box \bar{h}_{\mu\nu} = 0. \tag{2.18}$$

Equation (2.18) is similar to the wave equation. We will show in the next section that (2.18) has a plane wave solution which describes GWs. We can still simplify this equation by imposing a further coordinate transformation such that $\Box \xi_\mu = 0$ which keeps the Lorenz gauge condition fulfilled. This also implies $\Box \xi_{\mu\nu} = 0$ where $\xi_{\mu\nu} \equiv \partial_\mu \xi_\nu + \partial_\nu \xi_\mu + \eta_{\mu\nu} \partial_\rho \xi^\rho = 0$. The field equation (2.18) then become

$$\Box (\bar{h}_{\mu\nu} - \xi_{\mu\nu}) = 0. \tag{2.19}$$

We choose ξ^0 in order that the trace $\bar{h} = 0$, which then implies $\bar{h}_{\mu\nu} = h_{\mu\nu}$. So equation (2.18) reduces to

$$\Box h_{\mu\nu} = 0. \tag{2.20}$$

Moreover, we choose ξ^i such that $h^{0i} = 0$. Imposing these conditions, we can write the Lorenz gauge for $\mu = 0$ as $\partial^0 h_{00} = 0$. This shows that h_{00} is constant and time-independent. As GWs are the time-dependent part of the metric, it means $h_{00} = 0$. Bring it all together we have

$$h^{0\mu} = 0, \qquad h^i{}_i = 0, \qquad \partial^j h_{ij} = 0. \tag{2.21}$$

The conditions in (2.21) are known as transverse-traceless gauge or TT-gauge. Now we can do some counting. We have started with a symmetric perturbation $h_{\mu\nu}$ which has ten degrees of freedom. Imposing Lorenz gauge with four conditions, and also the transverse-traceless gauge with another four conditions, reduces the number of degrees of freedom to two which are the two polarization of a GWs.

2.2 Energy of GW

A source which emits GWs loses energy. We are interested in calculating this energy carried by the emitted GWs. Since there is no local energy-momentum tensor for GWs (Tong, 2019), there is no straight forward way to do so. In the linearized theory, we can define an energy-momentum non-tensor $t_{\mu\nu}$ such that $\partial^\mu t_{\mu\nu} = 0$. This, however, is not invariant under gauge transformations. Our approach is to expand the Einstein equation to the second order in $h_{\mu\nu}$

Version of August 18, 2021– Created August 18, 2021 - 10:17

$$\left[R_{\mu\nu} - \frac{1}{2}g_{\mu\nu}R\right]^{(1)} + \left[R_{\mu\nu} - \frac{1}{2}g_{\mu\nu}R\right]^{(2)} = \frac{8\pi G}{c^4}T_{\mu\nu}. \tag{2.22}$$

In each term, the superscript (n) specifies the order h^n. We can rewrite this as

$$\left[R_{\mu\nu} - \frac{1}{2}g_{\mu\nu}R\right]^{(1)} = \frac{8\pi G}{c^4}\left(T_{\mu\nu} + t_{\mu\nu}\right), \tag{2.23}$$

and consider the second order expansion to be the gravitational energy-momentum non-tensor $t_{\mu\nu}$,

$$\begin{aligned} t_{\mu\nu} &= -\frac{c^4}{8\pi G}\left[R_{\mu\nu} - \frac{1}{2}g_{\mu\nu}R\right]^{(2)} \\ &= -\frac{c^4}{8\pi G}\left[R^{(2)}_{\mu\nu} - \frac{1}{2}\eta_{\mu\nu}R^{(2)} - \frac{1}{2}h_{\mu\nu}R^{(1)}\right] \\ &= -\frac{c^4}{8\pi G}\left[R^{(2)}_{\mu\nu} - \frac{1}{2}\eta_{\mu\nu}R^{(2)}\right]. \end{aligned} \tag{2.24}$$

Where in the third equality we have used the fact that $R^{(1)}$ term vanishes at linear order by the equation of motion far from the source, $T_{\mu\nu} = 0$. Notably the bianchi identity in the linearized theory (2.14) implies that $\partial^\mu t_{\mu\nu} = 0$. We now need to expand the Ricci tensor to the second order

$$\begin{aligned} R^{(2)}_{\mu\nu} =& \frac{1}{2}h^{\rho\sigma}\partial_\mu\partial_\nu h_{\rho\sigma} - h^{\rho\sigma}\partial_\rho\partial_{(\mu}h_{\nu)\sigma} + \frac{1}{4}\partial_\mu h_{\rho\sigma}\partial_\nu h^{\rho\sigma} + \partial^\sigma h^\rho{}_\nu\partial_{[\sigma}h_{\rho]\mu} \\ &+ \frac{1}{2}\partial_\sigma\left(h^{\sigma\rho}\partial_\rho h_{\mu\nu}\right) - \frac{1}{4}\partial^\rho h\partial_\rho h_{\mu\nu} - \left(\partial_\sigma h^{\rho\sigma} - \frac{1}{2}\partial^\rho h\right)\partial_{(\mu}h_{\nu)\rho}. \end{aligned} \tag{2.25}$$

Substituting this in the expression (2.24), we can calculate $t_{\mu\nu}$. However, in order to obtain a physical tensor, we need to make it gauge invariant. The GWs has a characteristic length scale, we denote by λ. We take the average over the GW oscillations over some region V of typical size a

$$\left\langle t_{\mu\nu}\right\rangle \equiv \int_V d^4x\, W(x-y)t_{\mu\nu}(y). \tag{2.26}$$

Where the weighting function $W(x)$ varies smoothly over V with $\int_V d^4x W(x) = 1$ and $W(x) = 0$ on ∂V. The resulted $\left\langle t_{\mu\nu}\right\rangle$ is known as coarse-grained energy tensor. The averages of total derivatives scale as $\left\langle \partial X\right\rangle \sim 1/a$ and so it goes to zero for large a. We can also integrate by part inside the average and the total derivatives go to zero, $\left\langle X\partial Y\right\rangle = -\left\langle (\partial X)Y\right\rangle$. In

the transverse-traceless gauge, the averaged energy-momentum tensor become

$$\langle t_{\mu\nu} \rangle = \frac{c^4}{32\pi G} \langle \partial_\mu h_{\rho\sigma} \partial_\nu h^{\rho\sigma} \rangle. \tag{2.27}$$

We can prove this tensor is conserved

$$\partial^\mu \langle t_{\mu\nu} \rangle = \frac{c^4}{32\pi G} \langle (\Box h_{\rho\sigma}) \partial_\nu h^{\rho\sigma} + \frac{1}{2} \partial_\nu (\partial_\mu h_{\rho\sigma} \partial^\mu h^{\rho\sigma}) \rangle. \tag{2.28}$$

Where the first term vanishes based on the equation of motion and the second term is a total derivative and goes to zero for large a. Furthermore, we can verify that the residual gauge do not change this averaged energy-momentum tensor

$$\delta \langle t_{\mu\nu} \rangle = \frac{1}{16\pi G} \langle \partial_\mu h_{\rho\sigma} \partial_\nu (\partial^\rho \xi^\sigma + \partial^\sigma \xi^\rho) \rangle = 0. \tag{2.29}$$

First term vanishes by integrating by parts ∂^ρ, and using the Lorenz condition $\partial^\rho h_{\rho\sigma} = 0$. The second term vanishes in the same way. Therefore, taking $a \to \infty$, $\langle t_{\mu\nu} \rangle$ is gauge invariant. We can now compute the energy flux. The GW energy inside the volume V is

$$E_V = \int_V d^3x \, \langle t^{00} \rangle. \tag{2.30}$$

We obtain the energy flux by taking the time derivative of equation (2.30)

$$\begin{aligned} \frac{1}{c} \frac{dE_V}{dt} &= \int_V d^3x \, \partial_0 \langle t^{00} \rangle = - \int_V d^3x \, \partial_i \langle t^{i0} \rangle \\ &= - \int_S dA \, n_i \langle t^{0i} \rangle. \end{aligned} \tag{2.31}$$

Where in the second equality we have used the conservation law for averaged energy-momentum tensor which implies $\partial_0 \langle T^{00} \rangle + \partial_i \langle T^{i0} \rangle = 0$. We then applied divergence theorem in the third equality, where n^i is orthonormal to the surface S. If we assume a spherical surface far from the source, the surface element become $dA = r^2 d\Omega$, and $\hat{n} = \hat{r}$. Then we can write the energy flux as

$$\frac{dE}{dAdt} = c \, \langle t^{0r} \rangle, \quad \text{where } \langle t^{0r} \rangle = \frac{c^4}{32\pi G} \langle \partial^0 h_{ij}^{TT} \partial_r h_{ij}^{TT} \rangle. \tag{2.32}$$

Since decreasing of the total energy in the volume is equivalent to the energy carried by the outward-propagating GWs, $-dE_V = dE$, we have omitted the minus sign.

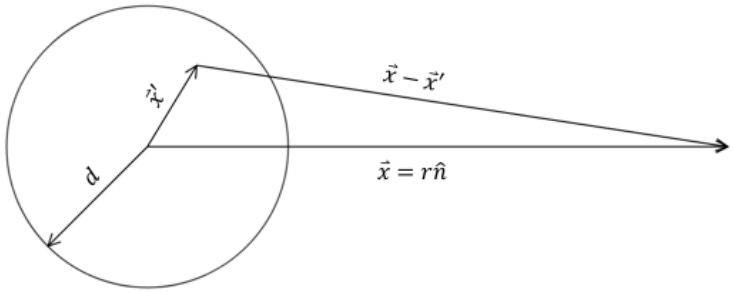

Figure 2.1: *A schematic representation of Equation (2.36).*

2.3 Plane waves

Now we try to solve the field equation (2.20) in the TT-gauge. One solution is provided by GW

$$h_{\mu\nu} = Re\left(e_{\mu\nu}e^{ik_\rho x^\rho}\right). \tag{2.33}$$

Here the $e_{\mu\nu}$ is a symmetric polarization tensor and the wave vector $k^\mu = (\omega/c, \mathbf{k})$ is a real 4-vector and satisfy $k^\mu k_\mu = 0$ which implies $\omega/c = \pm|\mathbf{k}|$. We can then conclude that the GWs in vacuum travel at speed of light. The lorenz gauge condition on a plane wave solution become $k^\mu e_{\mu\nu} = 0$ which shows that the polarization is transverse to the direction of propagation. If we assume that the wave is propagating in the z direction, $\mathbf{k} = (0, 0, \omega/c)$, the $h_{\mu\nu}$ can be written as

$$h_{ab}(t,z) = \begin{pmatrix} h_+ & h_\times \\ h_\times & -h_+ \end{pmatrix}_{ab} \cos[\omega(t - z/c)], \qquad (a,b) = (1,2). \tag{2.34}$$

where h_+ and $h_\times$ are known as plus and cross polarization of the GWs. This solution corresponds to a free wave coming in from infinity, and propagating to infinity. However, in reality GW sources emit waves at a finite distance from observer. We are interested in looking at the perturbation $h_{\mu\nu}$ far away from these sources. Equation (2.16) can be solved using retarded Green's function as

$$\bar{h}_{\mu\nu}(t,\mathbf{x}) = \frac{4G}{c^4}\int_V d^3x' \frac{T_{\mu\nu}(t_{\text{ret}},\mathbf{x}')}{|\mathbf{x}-\mathbf{x}'|}. \tag{2.35}$$

Here we denote $(t,\mathbf{x})$ and $(t_{\text{ret}},\mathbf{x}')$ as the observer and source coordinates as shown in Figure 2.1, and the retarded time as $t_{ret} = t - \frac{|\mathbf{x}-\mathbf{x}'|}{c}$. We assumed that the source is localized to V with a size of d. If $|\mathbf{x}-\mathbf{x}'| \gg d$,

we can approximate

$$|\mathbf{x}-\mathbf{x}'| = r - \frac{\mathbf{x}\cdot\mathbf{x}'}{r} + \ldots \to \frac{1}{|\mathbf{x}-\mathbf{x}'|} = \frac{1}{r} + \frac{\mathbf{x}\cdot\mathbf{x}'}{r^3} + \ldots \tag{2.36}$$

Here $r \equiv |\mathbf{x}|$. We can then approximate the retarded time t_{ret} in the energy-momentum tensor

$$T_{\mu\nu}(t_{\text{ret}}, \mathbf{x}') = T_{\mu\nu}\big(t - \frac{r}{c} + \frac{\mathbf{x}\cdot\mathbf{x}'}{cr} + \ldots, \mathbf{x}'\big). \tag{2.37}$$

We can further taylor expand argument (2.37) by assuming that the typical velocity of the source is non-relativistic. This assumption for a binary with characteristic frequency ω and hence an energy-momentum $T_{\mu\nu} \sim e^{i\omega t}$ becomes $\omega d \ll c$. So we have

$$T_{\mu\nu}(t_{\text{ret}}, \mathbf{x}') = T_{\mu\nu}(t - \frac{r}{c}, \mathbf{x}') + \dot{T}_{\mu\nu}(t - \frac{r}{c}, \mathbf{x}')\frac{\mathbf{x}\cdot\mathbf{x}'}{cr} + \ldots \tag{2.38}$$

So at the leading order in d/r in argument (2.35), we would have

$$\bar{h}_{\mu\nu}(t, \mathbf{x}) = \frac{1}{r}\frac{4G}{c^4}\int_V d^3x'\; T_{\mu\nu}(t - r/c, \mathbf{x}'), \tag{2.39}$$

from which we are more interested in the spatial components of the perturbation

$$\bar{h}_{ij}(t, \mathbf{x}) = \frac{1}{r}\frac{4G}{c^4}\int_V d^3x'\; T_{ij}(t - r/c, \mathbf{x}'). \tag{2.40}$$

For convenience, we introduce the second momenta of mass density or quadrupole moment of the energy,

$$M^{ij}(t) = \frac{1}{c^2}\int_V d^3x\; T^{00}(t, \mathbf{x})x^i x^j. \tag{2.41}$$

The second derivative of M^{ij} turns out to give the integration of energy-momentum density over the source region

$$\frac{1}{2}\ddot{M}^{ij}(t) = \int_V d^3x'\; T^{ij}(t, \mathbf{x}'). \tag{2.42}$$

To show this we start by taking the first derivative of M^{ij} defined in (2.41),

$$\begin{aligned} c^2\dot{M}^{ij} &= \int_V d^3x\; \partial_0 T^{00}x^i x^j = -\int_V d^3x\; \partial_k T^{k0}x^i x^j \\ &= \int_V d^3x\; T^{k0}\partial_k(x^i x^j) = \int_V d^3x\; (T^{i0}x^j + T^{j0}x^i). \end{aligned} \tag{2.43}$$

Here in the second equality we have used the conservation law for energy-momentum which implies $\partial_0 T^{00} + \partial_i T^{i0} = 0$. We then used integration by part in the third equality. We can now take the second derivative of quadrupole moment M^{ij},

$$\begin{aligned} c^2 \ddot{M}^{ij} &= \int_V d^3x \, (\partial_0 T^{i0} x^j + \partial_0 T^{j0} x^i) = -\int_V d^3x \, (\partial_k T^{ik} x^j + \partial_k T^{jk} x^i) \\ &= \int_V d^3x \, (T^{ik}\partial_k x^j + T^{jk}\partial_k x^i) = \int_V d^3x \, (T^{ik}\delta^j{}_k + T^{jk}\delta^i{}_k) = 2\int_V d^3x \, T^{ij}. \end{aligned} \tag{2.44}$$

Which prove our claim (2.42). We introduce the projection and Lambda operators as defined in (Weinberg, 1972), which allow us to transfer any tensor to TT-gauge.

$$P_{ij}(\hat{\mathbf{n}}) = \delta_{ij} - n_i n_j, \quad \Lambda_{ij,kl}(\hat{\mathbf{n}}) = P_{ik}P_{jl} - \frac{1}{2}P_{ij}P_{kl}, \quad h^{TT}_{ij} = \Lambda_{ij,kl}(\hat{\mathbf{n}})h_{kl}. \tag{2.45}$$

Considering the Lambda operators, equation (2.40), and (2.42) we may obtain the leading term of the perturbation in TT-gauge far from a non-relativistic source in terms of the quadrupole moment

$$h^{TT}_{ij} = \frac{1}{r}\frac{2G}{c^4}\Lambda_{ij,kl}(\hat{\mathbf{n}})\ddot{M}^{kl}(t - r/c) \tag{2.46}$$

Implementing the explicit expression for the Lambda operators we can calculate the perturbation for the GWs propagating in the z direction.

$$h^{TT}_{ij} = \frac{1}{r}\frac{2G}{c^4}\begin{pmatrix} (\ddot{M}_{11} - \ddot{M}_{22})/2 & \ddot{M}_{12} & 0 \\ \ddot{M}_{21} & -(\ddot{M}_{11} - \ddot{M}_{22})/2 & 0 \\ 0 & 0 & 0 \end{pmatrix}. \tag{2.47}$$

Which we may interpret the amplitudes of plus and cross polarization as defined in (2.34),

$$\begin{aligned} h_+ &= \frac{1}{r}\frac{G}{c^4}(\ddot{M}_{11} - \ddot{M}_{22}), \\ h_\times &= \frac{2}{r}\frac{G}{c^4}\ddot{M}_{12}. \end{aligned} \tag{2.48}$$

The incident GWs, on the other hand, can propagate in any direction with regard to the gravitational detector frame. To obtain the generalized plus and cross polarization for a GW travelling in a generic direction $\hat{n}$, we need to describe the propagation direction in the detector frame. A convenient way is to relate the z-direction of the detector frame to the propagation

Version of August 18, 2021– Created August 18, 2021 - 10:17

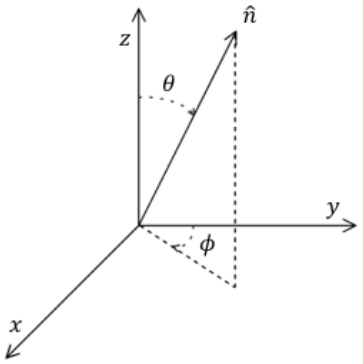

Figure 2.2: *The projection of a generic propagation direction $\hat{n}$, on the $(\hat{x}, \hat{y}, \hat{z})$ frame. θ is the angle formed by $\hat{n}$ with $\hat{z}$; ϕ is the angle formed by the projection of the $\hat{n}$ on the $x - y$ plane, with $\hat{x}$, and $\hat{y}$.*

direction by performing a rotation. Similarly the second mass moment tensor will transform as $M \to \mathcal{R}^T M \mathcal{R}$. Where the rotation matrix $\mathcal{R}$ is

$$\mathcal{R} = \begin{pmatrix} \cos\phi & \sin\phi & 0 \\ \sin\phi & \cos\phi & 0 \\ 0 & 0 & 1 \end{pmatrix} \begin{pmatrix} 1 & 0 & 0 \\ 0 & \cos\theta & \sin\theta \\ 0 & -\sin\theta & \cos\theta \end{pmatrix}. \tag{2.49}$$

As illustrated in Figure 2.2, this involves a rotation in the direction of the orbital phase ϕ, and another in the direction of the inclination θ. Applying the transformation on the second mass momenta tensor, we can calculate the generalized plus and cross polarization as,

$$\begin{aligned} h_+(t;\theta,\phi) = \frac{1}{r}\frac{G}{c^4}\Big(& \ddot{M}_{11}\left(\cos^2\phi - \sin^2\phi\cos^2\theta\right) + \ddot{M}_{22}\left(\sin^2\phi - \cos^2\phi\sin^2\theta\right) \\ & - \ddot{M}_{33}\sin^2\theta - \ddot{M}_{12}\sin 2\phi(1+\cos^2\theta) + \ddot{M}_{13}\sin\phi\sin 2\theta + \ddot{M}_{23}\cos\phi\sin 2\theta\Big), \\ h_\times(t;\theta,\phi) = \frac{1}{r}\frac{G}{c^4}\Big(& \left(\ddot{M}_{11} - \ddot{M}_{22}\right)\sin 2\phi\cos\theta + 2\ddot{M}_{12}\cos 2\phi\cos\theta - 2\ddot{M}_{13}\cos\phi\sin\theta \\ & + 2\ddot{M}_{23}\sin\phi\sin\theta\Big). \end{aligned} \tag{2.50}$$

Using the expression (2.46) and (2.32), we can calculate the energy flux of the GWs far from the source,

$$\frac{dE}{dAdt} = \frac{c^5}{32\pi G}\langle \partial^0 h_{ij}^{TT} \partial_r h_{ij}^{TT} \rangle. \tag{2.51}$$

We are now able to calculate the radial derivative of the perturbation

$$\begin{aligned}\partial_r h_{ij}^{TT} &= -\frac{1}{r^2}\frac{2G}{c^4}\Lambda_{ij,kl}(\hat{\mathbf{n}})\ddot{M}^{kl}(t-r/c) + \frac{1}{r}\frac{2G}{c^4}\Lambda_{ij,kl}(\hat{\mathbf{n}})\partial_r\ddot{M}^{kl}(t-r/c)\\ &\simeq \frac{1}{r}\frac{2G}{c^4}\Lambda_{ij,kl}(\hat{\mathbf{n}})\frac{-1}{c}\partial_t\ddot{M}^{kl}(t-r/c)\\ &= \frac{1}{r}\frac{2G}{c^4}\Lambda_{ij,kl}(\hat{\mathbf{n}})\partial^0\ddot{M}^{kl}(t-r/c) = \partial^0 h_{ij}^{TT},\end{aligned} \tag{2.52}$$

where we have neglected $O(1/r^2)$ in the second equality. We are now able to write the expression for the energy flux of the GW

$$\frac{dE}{dAdt} = \frac{c^3}{32\pi G}\langle \dot{h}_{ij}^{TT}\dot{h}_{ij}^{TT}\rangle. \tag{2.53}$$

We can rewrite the result in terms of plus h_+ and cross $h_\times$ polarization,

$$\frac{dE}{dAdt} = \frac{c^3}{16\pi G}\langle \dot{h}_+^2 + \dot{h}_\times^2\rangle. \tag{2.54}$$

We can also find an expression for the radiated power per unit solid angle by rewriting $dP = dE/dt$, and $dA = r^2 d\Omega$ in (2.54),

$$\frac{dP}{d\Omega} = \frac{r^2 c^3}{16\pi G}\langle \dot{h}_+^2 + \dot{h}_\times^2\rangle. \tag{2.55}$$

2.4 Binary Inspiral: circular orbit

Consider a system consisting of two WDs with mass m_1 and m_2 in close orbit around each other. We choose the origin for the coordinate system to be the WDs' center of mass. Doing so, we can describe the motion of two bodies to an equivalent one-body problem with mass $\mu = m_1 m_2/(m_1+m_2)$ known as reduced mass. It is worth noting that we ignore frictional losses. Without loss of generality we can consider circular orbits for double WDs. GWs are emitted most strongly at periastron for elliptical orbits. This radiation reaction slows the motion and hence the orbit circularizes (Glampedakis & Kennefick, 2002). Therefore, circular orbits are expected. Assuming the relative coordinate is performing a circular motion in the $x-y$ plane, we have

$$x_0 = R\cos\Big(\omega_s t + \frac{\pi}{2}\Big), \quad y_0 = R\sin\Big(\omega_s t + \frac{\pi}{2}\Big), \quad z_0 = 0. \tag{2.56}$$

Where we added the phase $\frac{\pi}{2}$ to obtain a positive sign for perturbation later. If we treat the WDs as point particles (Broek et al., 2012), then the energy density can be written as

$$T^{00}(t,\mathbf{x}) = \mu\delta\big(x + R\sin\omega_s t\big)\delta\big(y - R\cos\omega_s t\big)\delta(z). \tag{2.57}$$

Implementing above in (2.41) we can calculate the quadrupole moment M^{ij} for this system,

$$M^{ij}(t) = \int d^3x\ \mu\delta\big(x - x_0\big)\delta\big(y - y_0\big)\delta(z - z_0)x^i x^j = \mu x_0^i(t)y_0^j(t). \tag{2.58}$$

Which results in

$$M^{ij} = \mu R^2 \begin{pmatrix} \sin^2\omega_s t & -\sin\omega_s t\cos\omega_s t & 0 \\ -\sin\omega_s t\cos\omega_s t & \cos^2\omega_s t & 0 \\ 0 & 0 & 0 \end{pmatrix}. \tag{2.59}$$

Putting the quadruple expression above in (2.50), the cross and plus polarization modes can be represented as

$$\begin{aligned} h_+(t;\theta,\phi) &= \frac{4}{r}\frac{G}{c^4}\mu R^2\omega_s^2\left(\frac{1+\cos^2\theta}{2}\right)\cos\big(2\omega_s t_{ret} + 2\phi\big), \\ h_\times(t;\theta,\phi) &= \frac{4}{r}\frac{G}{c^4}\mu R^2\omega_s^2\cos\theta\sin\big(2\omega_s t_{ret} + 2\phi\big). \end{aligned} \tag{2.60}$$

From which we can conclude that the angular frequency of quadrupole radiation is twice the orbital angular frequency of the binary. We now use Kepler's third law to eliminate R in favor of ω_s,

$$\omega_s^2 = \frac{G(m_1+m_2)}{R^3}. \tag{2.61}$$

Introducing the **chirp mass** of the binary system $M_c \equiv \mu^{3/5}(m_1+m_2)^{2/5}$, we can combine the mass dependant parameters and then we can express the plus and cross polarization modes of the GWs (2.60) emitted by the binary system in terms of its chirp mass, distance, and the frequency as,

$$\begin{aligned} h_+(t;\theta,\phi) &= \mathcal{A}\ \frac{1+\cos^2\theta}{2}\cos\big(2\pi f t_{ret} + 2\phi\big), \\ h_\times(t;\theta,\phi) &= \mathcal{A}\ \cos\theta\sin\big(2\pi f t_{ret} + 2\phi\big), \end{aligned} \tag{2.62}$$

where the dimensionless GW strain $\mathcal{A}$ is defined as

$$\mathcal{A} = \frac{4}{rc^4}\big(GM_c\big)^{5/3}\big(\pi f\big)^{2/3} \simeq 6\times10^{-20}\left(\frac{1\text{kpc}}{r}\right)\left(\frac{M_c}{\text{M}_\odot}\right)^{5/3}\left(\frac{f}{1\text{Hz}}\right)^{2/3}, \tag{2.63}$$

and **GW frequency** is expressed as $f = 2\omega_s/2\pi$. Substituting the above expression for the GWs polarization (2.62) into (2.55), we can calculate the radiated power per solid angle by the GWs

$$\frac{dP}{d\Omega} = \frac{2}{\pi}\frac{c^5}{G}\left(\frac{GM_c\pi f}{c^3}\right)^{10/3}\left[\left(\frac{1+\cos^2\theta}{2}\right)^2 + \cos^2\theta\right]. \tag{2.64}$$

We used the fact that $\left\langle \cos^2(2\pi f t_{ret} + 2\phi)\right\rangle = \left\langle \sin^2(2\pi f t_{ret} + 2\phi)\right\rangle = 1/2$. By integrating over the solid angle, we can compute the total radiated power carried out by GWs from a pair of WDs spiralling in towards each other

$$P_{GW} = \frac{32}{5}\frac{c^5}{G}\left(\frac{GM_c\pi f}{c^3}\right)^{10/3}. \tag{2.65}$$

If we neglect the frictional loss, the orbital energy loss is radiated away completely by GWs, $\dot{E}_{orbit} = P_{GW}$. We would then have

$$-\frac{d}{dt}\left(\frac{Gm_1m_2}{2R}\right) = \frac{32}{5}\frac{c^5}{G}\left(\frac{GM_c\pi f}{c^3}\right)^{10/3}. \tag{2.66}$$

Again we use the Kepler's third law to eliminate R and its derivative $\dot{R}$, in favor of the GW frequency f and its derivative $\dot{f}$. As a result, we get

$$\dot{f} = \frac{96}{5}\pi^{8/3}\left(\frac{GM_c}{c^3}\right)^{5/3} f^{11/3}. \tag{2.67}$$

Consider at the time of coalescence t_{coal}, the frequency diverges. Then by integrating (2.67) over time, we obtain the explicit expression for the frequency of the GW emitted by our binary system in terms of the chirp mass M_c, and the time to coalescence $\tau \equiv t_{coal} - t$

$$f \simeq 151\,\mathrm{Hz}\left(\frac{\mathrm{M}_\odot}{M_c}\right)^{5/8}\left(\frac{1\mathrm{s}}{\tau}\right)^{3/8}. \tag{2.68}$$

We can estimate that for a typical WD binary, each star with a mass of $0.7M_\odot$, the chirp mass is $M_c = 0.61M_\odot$. LISA detects GWs in a frequency range of $[10^{-4}, 1]\,Hz$. Consequently, using (2.68) this system of two stars can be detected in time to coalescence range of around $[0, 2]\,Gyr$. In other words, the emitted GWs from this binary will be detectable by LISA for a period of roughly 2 Gyr prior to merger. When merging stars approach closer to each other, the flat background assumption becomes invalid, and we must replace it with the Scwartzschild background, which

establishes a boundary for the minimum radial distance at which a stable circular orbit can exist. This innermost stable circular orbit is located at $r = 6G(m_1 + m_2)/c^2$. Below this orbital distance, the stars begin to merge, necessitating a different set of considerations. We can use Kepler's law to demonstrate that this limitation imposes a maximum for the above-calculated frequency (2.68).

$$f_{max} = 2.2\,\text{kHz}\left(\frac{M_\odot}{m_1 + m_2}\right). \tag{2.69}$$

For the above binary, we have $f_{max} \sim 3600$ Hz. Using the theoretical maximum mass that a WD star might have, known as the Chandrasekhar mass, for both WDs in the binary, we find a maximum frequency of $f_{max} \sim 800$ Hz. Then we may conclude that all of the DWDs will merge long enough after passing through the LISA frequency range for the estimated waveform above to be valid. We can also understand why the LIGO sensitivity range is unsuitable for detecting DWDs in GWs.
We use a distance of 10 kpc to calculate the GW amplitude for a typical DWD system in the LISA frequency range. This amplitude is very tiny, in the range of 10^{-23} to 10^{-21}, making the detection challenging. Furthermore, the total power radiated away by GW from this binary at mHz frequency is around 2.1×10^{27} watts. In comparison, this is almost ten times greater than the total emitted power from the Sun.

2.5 Signal Detection

It is estimated that the GW signal will be buried in considerably greater noise in the present detectors (Maggiore, 2007). The typical method for recovering signals from the coalescence of compact binaries is to use optimal matched filtering with theoretically predicted waveform templates. Following the selection of the best-fitting template, the confidence of this method is characterized by the signal to noise ratio of the data. The signal to noise ratio (SNR) for a typical DWD detectable in LISA averaged over sky location, polarization, and inclination is given by (Robson et al. 2019)

$$\rho^2 = \mathcal{A}^2 \frac{T_{LISA}}{S_n(f)}, \tag{2.70}$$

where $\mathcal{A}$ is the amplitude of GW signal defined in (2.63), T_{LISA} is the LISA mission life time, and $S_n(f)$ is the power spectral density (PSD) of the detector noise. As numerous templates are considered in data analysis,

the SNR threshold has to be set to a quite large value 7 in order to avoid false alarms (e.g. Korol et al., 2020). The total PSD of the detector noise can be noted as the sensitivity curve and be expressed as (Robson et al., 2019)

$$S_n(f) = \frac{10}{3L^2}\left(S_{shot}(f) + \frac{4S_{acc}(f)}{(2\pi f)^4}\right) \times \frac{1}{\mathcal{R}(f)} + S_c(f), \tag{2.71}$$

where $L = 2.5$ Gm is the arm length of the LISA. We shall now explain each components of the sensitivity curve of the LISA. LISA arm lengths will fluctuate significantly during the mission ($\sim$3 percent of total arm Length). This large mismatch in arm lengths produces a frequency noise that is many orders of magnitude higher than the expected signal (McKenzie et al., 2009). To reduce the signal noise, the armlocking technique will be adopted for LISA. This technique locks the laser frequency to the length of the LISA arm. However, it also generates two types of other noises:

- **Shot noise** is a phase error in the signal received from a distant spacecraft caused by stochastic fluctuations due to the discrete nature of the field. The shot noise is estimated to be

$$S_{shot}(f) = (15 \text{ pm})^2 \text{ Hz}^{-1}. \tag{2.72}$$

- The spacecrafts are designed to move drag-free around the test masses. However, controlling the relative location of the spacecraft and the test mass causes the **acceleration noise** in the laser beam that travels between the spacecrafts. The acceleration noise is approximated as

$$S_{acc}(f) = \left(3 \times 10^{-15} \text{ m/s}^2\right)^2 \left(1 + \left(\frac{0.4 \text{ mHz}}{f}\right)^2\right) \text{Hz}^{-1}. \tag{2.73}$$

The transfer function $\mathcal{R}(f)$ in (2.71) relates the amplitude spectral density of the wave $S_h(f)$, and the spectral density of the signal recorded in the detector $S_s(f)$, by $S_s(f) = S_h(f)\mathcal{R}(f)$. However, it was decided to include its inverse in the noise spectral density rather than the signal. This function is numerically calculated in Larson et al. (2000) and well-fitted by the expression:

$$\mathcal{R}(f) = \frac{3}{10}\left(1 + \frac{6}{10}\left(\frac{f}{19.09 \text{ mHz}}\right)^2\right)^{-1}. \tag{2.74}$$

The last contributor to the sensitivity curve, $S_c(f)$, stems from unresolved Galactic binaries, which generate a time-varying confusion noise foreground.

Version of August 18, 2021– Created August 18, 2021 - 10:17

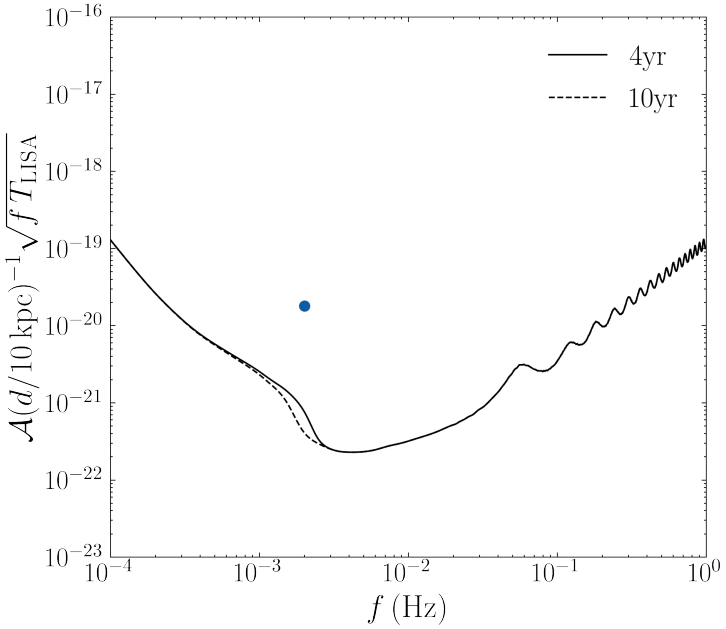

Figure 2.3: *The characteristic strain and frequency of a typical DWD with an orbital period of $T = 1000$ s, and a chirp mass of $M_c = 0.61 M_\odot$ placed at $d = 10$ kpc, indicated by a blue point. Solid and dashed lines show the sensitivity curve in terms of characteristic strain for the mission duration time of 4 and 10 years, respectively.*

Cornish & Robson (2017) analyzed a population of Galactic binaries to forecast this noise. They created the unresolved population by iteratively removing detected sources with SNR > 7, which is the nominal LISA SNR threshold. They then estimated the power spectral density of the residual signal as

$$S_c(f) = 1.80 e^{-44} f^{-7/3} e^{-f^{\alpha}+\beta f \sin(\kappa f)} \left(1 + \tanh\left(\gamma(f_k - f)\right)\right) \mathrm{Hz}^{-1}, \quad (2.75)$$

where for a mission duration of 4 yr, $\alpha = 0.138$, $\beta = -221$, $\kappa = 521$, $\gamma = 1680$, $f_k = 0.00113$. To account for maintenance operations and data gaps, we use a 75% duty cycle computed by the LISA pathfinder mission (estimated by LISA consortium). As a result, we must rescale the observation duration by a factor of 3/4. In Figure 2.3, the characteristic strain of LISA sensitivity curve $h_n = \sqrt{f S_n(f)}$, and that of the typical DWD $h_c = \mathcal{A}\sqrt{f T_{LISA}}$ with a chirp mass of $M_c = 0.61\,\mathrm{M}_\odot$, orbital period of 1000 s, and at a distance of 10 kpc are shown. The binary is detectable because it appears above the sensitivity curve. Based on (2.62), the phase component in the plus and cross polarization modes may be used to di-

rectly detect the GW frequency, f. The chirp mass of the coalescing object M_c can be described in terms of the GW frequency f, and its derivative $\dot{f}$, as can be seen in (2.67). Therefore, the chirp mass can be calculated by combining the derivative of GW frequency, which is challenging to measure for low-frequency ($< 1\,\text{mHz}$) slowly evolving sources, with the observed frequency. Now that we have the chirp mass, we can use the plus and cross GW strain in (2.62) to calculate the luminosity distance r and binary orbital inclination angle θ.

Chapter 3

Methods

In order to study the detectable DWDs in the MW Galactic halo, we first need to have a distribution of these binaries. However, only a few DWDs, typically mass transferring ones, have been detected in EM radiation. Therefore, we have to rely on the binary population synthesis method. This chapter introduces the binary population synthesis model that provides us DWDs' properties, then combines it with a cosmological simulation of MW-like halos to create a model that allows us to predict MW Galactic halo properties. Finally, we present a simulation of the Sgr satellite and use our technique to investigate its detectability in LISA.

3.1 Synthetic population of DWDs

In this work, we take advantage of a binary population synthesis model of DWDs provided by Toonen et al. (2017), which has been calibrated using observations and represents the properties of binary populations in our Galaxy well. This model is constructed from a population of Zero-age Main Sequence Stars (ZAMS) in binaries, assuming a binary fraction of 50% (Nelemans et al., 2001a). The mass of primary stars m_1 are drawn from a Kroupa initial mass function (IMF) (Kroupa, 2001) in the range of [0.95 $M_\odot$, 10 $M_\odot$]. For secondary stars m_2, they use a uniformly drawn mass in the range of [0.08 $M_\odot$, m_1] (Duchêne & Kraus, 2013). They adopt a uniform distribution in log space for the initial orbital separations (Abt, 1983) with an upper boundary of $10^6 R_\odot$, and a Maxwell-Boltzmann distribution in the range of [0, 1] for the initial eccentricity (Heggie, 1975).

They performed the binary population synthesis code `SeBa` (Portegies Zwart & Verbunt, 1996; Toonen et al., 2012) ultimately resulting in

$N = 901078$ DWDs, which represent a total mass of $2.28 \times 10^7 M_\odot$, with metallicity of $Z = 0.0001$ – appropriate for MW satellites – to evolve stars from the ZAMS until remnant formation, tracking the systems that form DWD binaries. They treat the common envelope phase by employing a $\gamma\alpha$ formalism (Zorotovic et al., 2011). It is worth mentioning that Korol et al. (2020) demonstrated metallicity has a limited impact on the DWD evolution. Throughout the evolution, they processed the interactions between the components of each binary, such as stellar winds, mass transfer, angular momentum loss, common envelope, magnetic braking, and gravitational radiation. After the formation of a DWD binary, we assume that it only loses energy due to GW emission. As a result, by adopting a circularized orbit, we may evolve its orbital separation using Equation (2.68) and find its orbital properties at a given time.

The mass transfer may occur before merging time in some binaries, resulting in a fast merger (Marsh et al., 2004). When the star radius in a binary system exceeds its Roche lobe, the matter outside this region will fall onto the companion star. The approximate Roche lobe for a star in a binary system is calculated by (Eggleton, 1983)

$$r_1 = R\frac{0.49q^{2/3}}{0.6q^{2/3} + log(1+q^{1/3})}, \tag{3.1}$$

where q is the mass ratio $q = m_1/m_2$, and R is the orbital separation. In this work, we assume that a binary has merged through the evolution if their radii exceed their Roche lobe.

Different progenitor mass and binary evolution channels result in different subtypes of DWDs based on their core composition. Indicating different core compositions, He (helium), CO (carbon/oxygen), and ONe (oxygen/neon) for WDs, we can classify the binaries as

- CO-CO: They account for 75% of our binary population. They have a relatively larger orbital separation at the DWD formation time, making them less relevant for LISA. Although, as they form fast, they account for the majority of DWDs with short orbital periods in a relatively short time (less than a Gyr). They have a median chirp mass of 0.61 $M_\odot$ (and a minimum of 0.37 $M_\odot$).

- CO-He: 8% of our binary population consists of binaries, in which one star is CO type, and the other has a He core composition. They have a median chirp mass of 0.43 $M_\odot$ (and a minimum of 0.22 $M_\odot$), and their formation takes about 2 Gyr.

Version of August 18, 2021– Created August 18, 2021 - 10:17

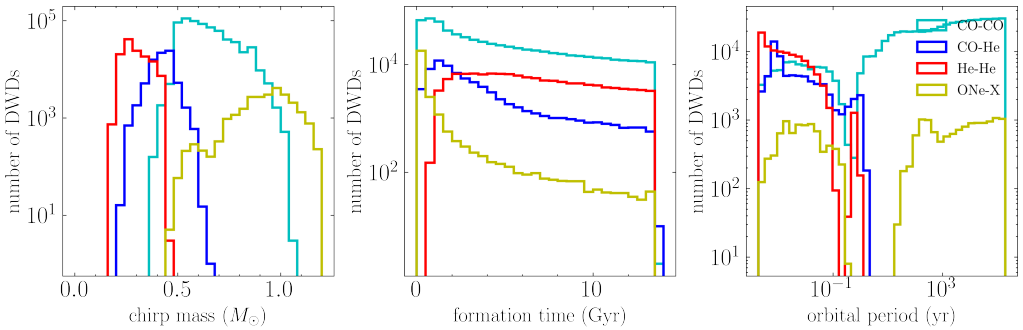

Figure 3.1: *The chirp mass (left), the formation time (middle), and the orbital period at the time of formation is illustrated for different subtypes of DWD.*

- He-He: Our binary population is made up of 14% of low mass binaries with a median chirp mass of 0.3 $M_\odot$. They take a relatively long time to form, about 6 Gyr.

- ONe-X: Only 3% of our binary population consists of binaries with at least one star with ONe core composition. They form relatively fast and are typically rare.

Now to get more insight into the binary population, we would like to visualize some of its physical properties. Figure 3.1 shows how different DWD subtypes differ in terms of formation time, chirp mass, and orbital period at their formation time. From time zero to 14 Gyr, in 100 steps, we find the contribution of binaries that has formed and not merged yet. In Figure 3.2 we demonstrate the contribution of different subtypes to the total number of DWDs at five different times. Figure 3.3 shows the chirp mass and orbital periods of DWDs at three different times. Finally, assuming a distance of 10 kpc for the DWDs in the synthetic population, Figure 3.4 shows the characteristic strain and frequency as well as the histogram of the chirp mass of DWDs at three different times.

3.2 Simulated Galactic halo

We use a publicly available suite of simulated Galactic halos by Bullock & Johnston (2005). They construct the MW-like halos by modeling a series of accretion events initiated in a cosmological context based on the extended Press-Schechter formalism (Lacey & Cole, 1993). By calculating the expected mass accretion rate of dark matter and assuming a cold baryonic mass fraction of $f = 0.02$, they determine the baryonic component in each

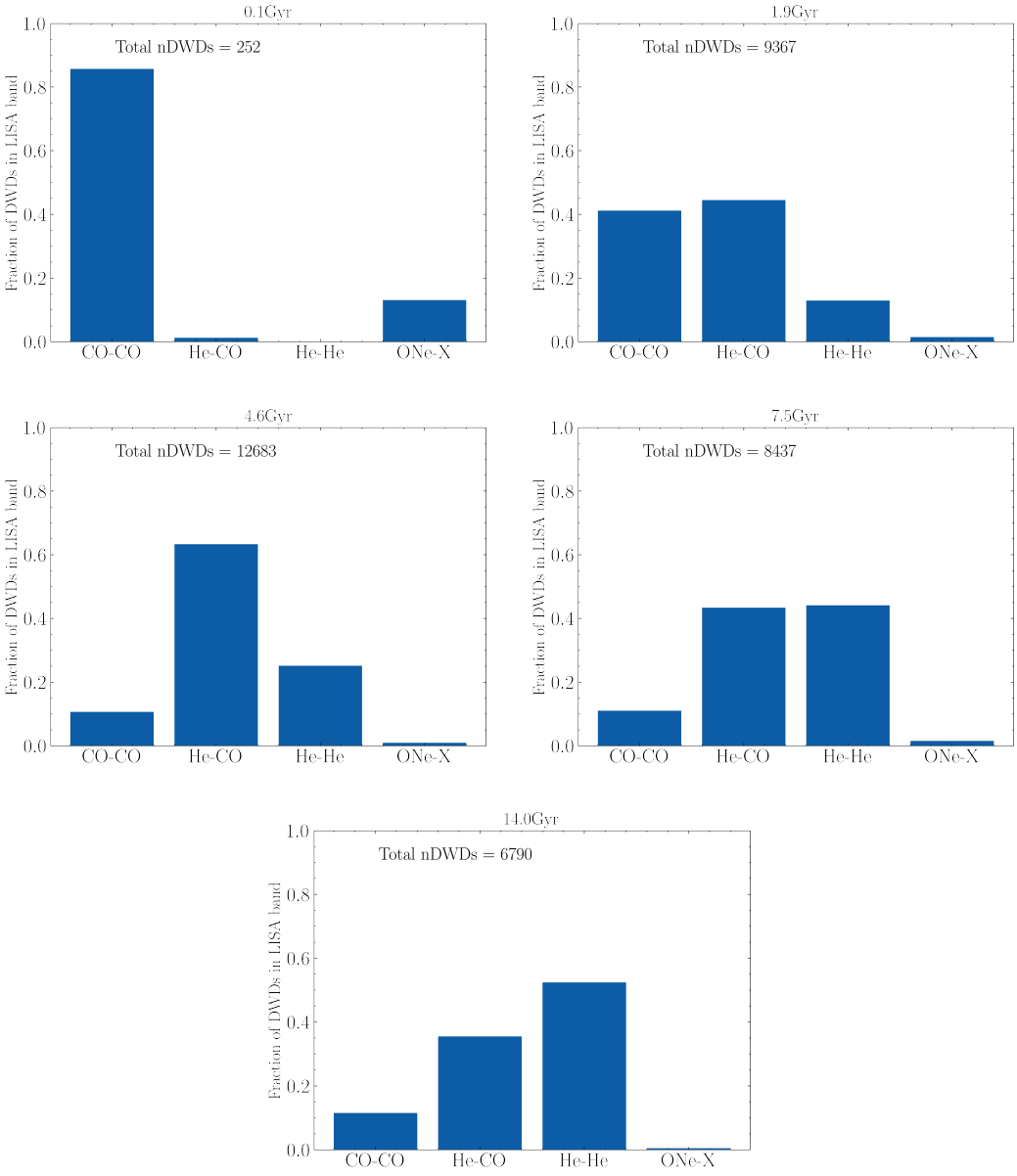

Figure 3.2: *Contribution of DWDs with different core composition in time. The CO-CO binaries are dominant at first (0.1 Gyr, top left), then the He-CO binaries take over at 1.9 Gyr (top right) and grow until 4.9 Gyr (middle left). After that, the gap between He-CO and He-He contribution decreases until, at 7.5 Gyr (middle right), He-He binaries become the dominating type. Their contribution increases until 14.0 Gyr (bottom). The total number of DWDs at each time is indicated in the panel.*

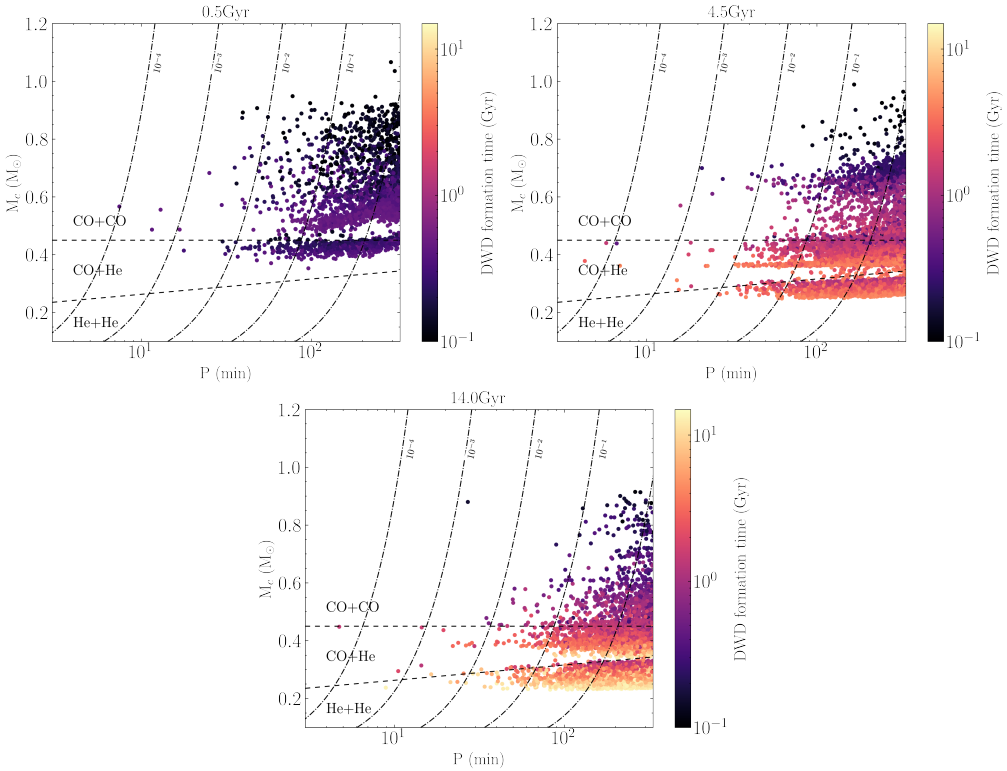

Figure 3.3: *Orbital period P and chirp mass M_c of DWDs in the LISA sensitivity range at three different times. Each point indicates a DWD which its formation time is shown on the color bar. The dashed-dotted lines show the time to coalescence in Gyr, and the dashed lines represent the approximate boundaries between different types of DWDs based on their core composition. At younger ages, the CO-CO binaries, as expected, dominate the population of the high-frequency DWDs (top panel). At later times (middle and bottom panel), He-CO and He-He binaries contribute to the high frequency DWDs which are relevant for LISA.*

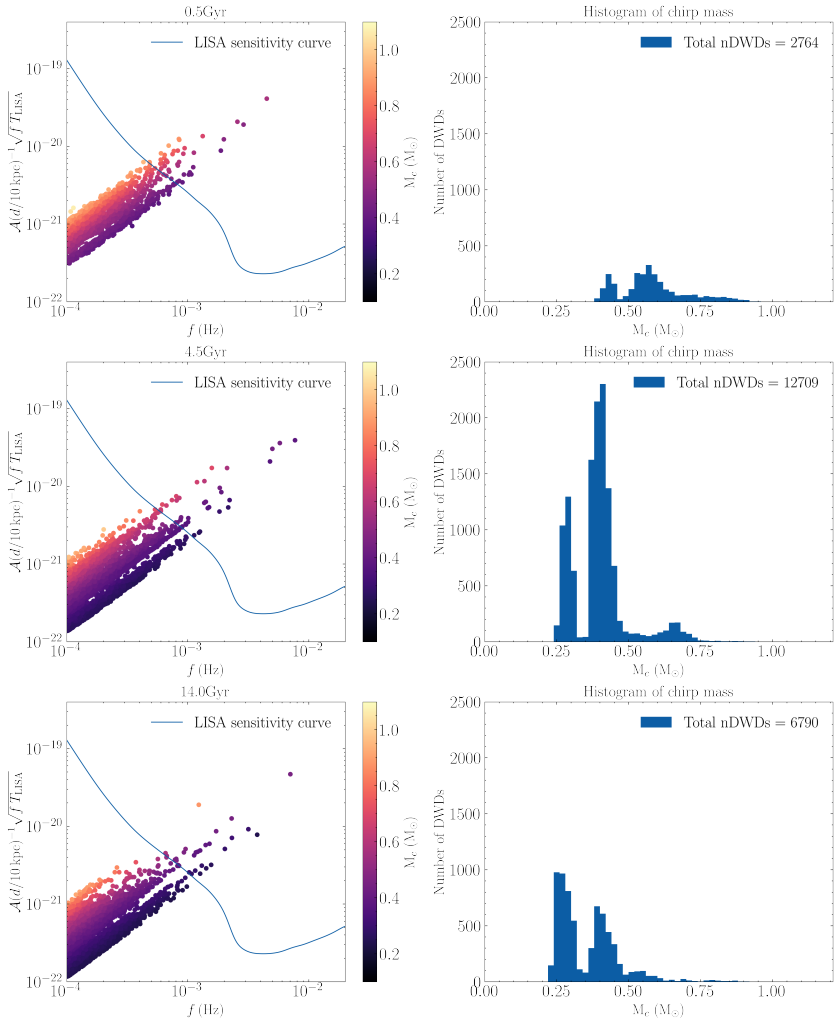

Figure 3.4: *Left panels show the characteristic strain of population of DWDs located at a distance of 10 kpc and their frequency f at three different times. Binaries that lay above the blue curve indicating LISA sensitivity curve, has a SNR>1, thus may be detectable. we observe that DWDs with a larger chirp mass – shown in the color bar – have a larger GW strain at each frequency bin. Furthermore, we find that low mass binaries contribute to the observable DWDs by LISA at later ages. Right panel shows the histogram of the chirp mass of DWDs. In the center right panel, the peaks from low to high masses are associated with He-He, He-CO, and CO-CO binaries. We see in the top right panel that He-He binaries do not contribute to younger population of DWDs.*

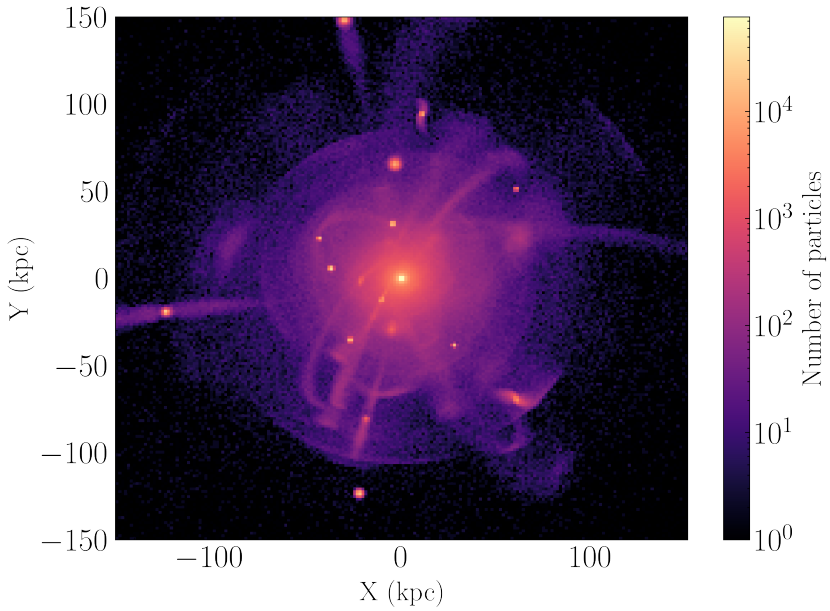

Figure 3.5: *The density map of simulated particles in halo 02.*

satellite. They adopt an average star formation timescale of $t_\star = 15$ Gyr to estimate the stellar mass of each satellite, then distribute it in the satellite by the spherically symmetric King profile (King, 1962). Finally, they track the disruption of satellites within a Navarro-Frenk-White (NFW, (Navarro et al., 1996)) potential using a high-resolution N-body simulation. They created 11 different Galactic halos, the validity of which is demonstrated by effectively reproducing observed structural properties of MW satellites such as luminosity function, luminosity-velocity dispersion relation, and surface brightness distribution. There is a substantial variance in the global properties of the resulted simulated halos as a result of the stochastic nature of hierarchical structure formation.

In their simulations they assume a ΛCDM cosmology with $\Omega = 0.3, \Omega_\Lambda = 0.7$, $\Omega_b h^2 = 0.024$, $h = 0.7$, $\sigma_8 = 0.9$. For each simulated halo, we get the position, age, and mass of every star particle from this simulation. The density map of halo 02 is illustrated in Figure 3.5. Figure

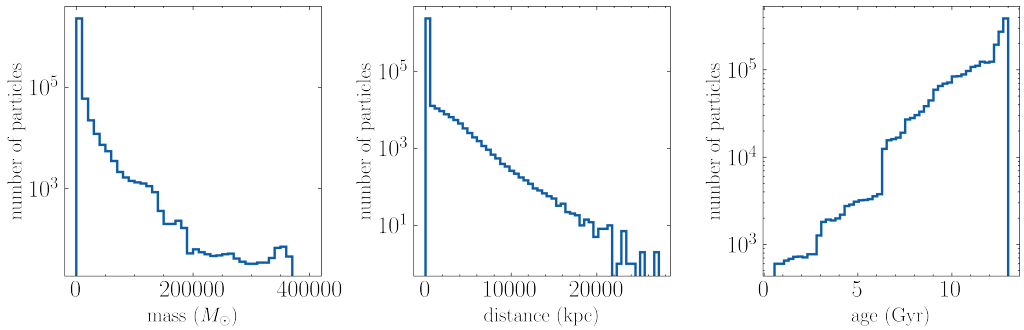

Figure 3.6: *Distribution of the mass (left), the distance (middle), and the age(right) of the simulation particles in a the halo 02 is shown.*

3.3 Combination of binary and Galactic halo models

In order to find the population of DWDs in the MW Galactic halo, we combine the binary population synthesis with our simulated halos following the methodology presented in Korol et al. (2020). We select stellar particles in simulated halos as the progenitors of DWDs and assign N_{DWD} DWDs drawn randomly from the synthetic population proportional to the mass of the simulation particles $M_\star$

$$N_{DWD,\star} = \frac{N_{DWD,SeBa}}{M_{SeBa}} M_\star = 0.039 \text{ DWD}/M_\odot, \tag{3.2}$$

where the fraction is determined by dividing the total number of DWD in our synthetic population $N_{DWD,SeBa}$ by the total mass it represents M_{SeBa}. The DWDs in the sample inherit the position and formation time of the progenitor simulated particle. We then evolve their orbits for the age of their progenitor simulated particle, removing any binaries that have yet to be formed or have already merged. Finally, we have the population of DWDs in the Galactic halos. With the chirp mass, distance, and the orbital period for each DWD, we can calculate its GW strain using Equation (2.63). The SNR is then calculated for the binaries with a frequency above 10^{-4} Hz, by Equation (2.70), and those binaries with SNR > 7 are kept as detectable DWDs.

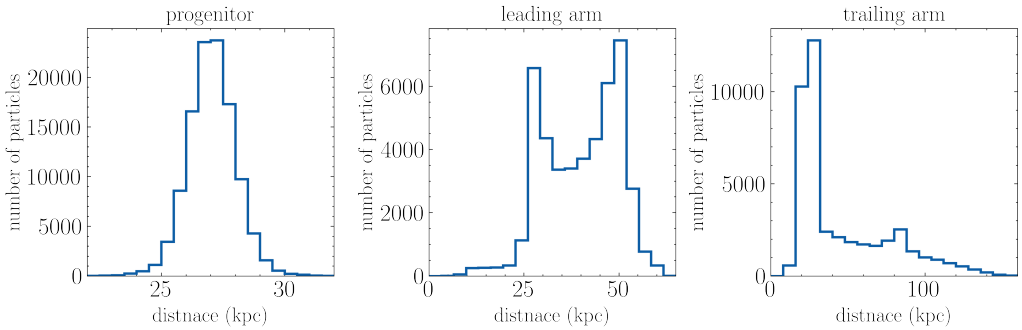

Figure 3.7: *Histogram of the simulation particle distance for the progenitor (left), the leading arm (middle), and the trailing arm(right) of the Sgr.*

3.4 Simulated Sagittarius

Similar to the Galactic halo, we require the three parameters position, mass, and age to combine with the synthetic population in order to find the population of DWDs in the Sgr satellite. We recover the positions and masses from the simulation provided by Vasiliev et al. (2021). They model the disruption of a spherical dark halo with an embedded stellar mass distribution following from King profile with an initial stellar mass of $2 \times 10^8 M_\odot$ and a halo mass $18\times$ larger. They first find the time-dependent perturbed potential of the MW + Large Magellanic Cloud (LMC) with a mass of $1.5 \times 10^{11} M_\odot$ using `Gyrfalcon` code and then track the evolution of Sgr within the pre-calculated combined potential by an N-body simulation. They adopt 2×10^5 particles of each light and dark matter component of the Sgr satellite. The simulations are carried for 2.5 orbital periods (3 Gyr) and indicate that nearly half of the stellar mass gets stripped to the present time. For verification of their model, they demonstrate that it can fit most of the observed Sgr remnant.

We divide the simulated Sgr into three components: the progenitor (bounded to the satellite), the leading arm, and the trailing arm. Figure 3.7 shows the distance distribution for the simulation particles of the Sgr galaxy. We use the definition of the right-handed celestial coordinate system Λ, B from Vasiliev et al. (2021). The center of the Sgr progenitor is located at $\Lambda = 0$. Positive and negative Λ correspond to the leading and the trailing arms, respectively, as shown in Figure 3.9.

de Boer et al. (2015) estimated the star formation history (SFH) of the Sgr streams using the Sloan Digital Sky Survey (SDSS) observational data within the stripe 82 region. They compare the observed Color Magnitude Diagrams (CMD) to a grid of synthetic CMDs to determine the SFH in the

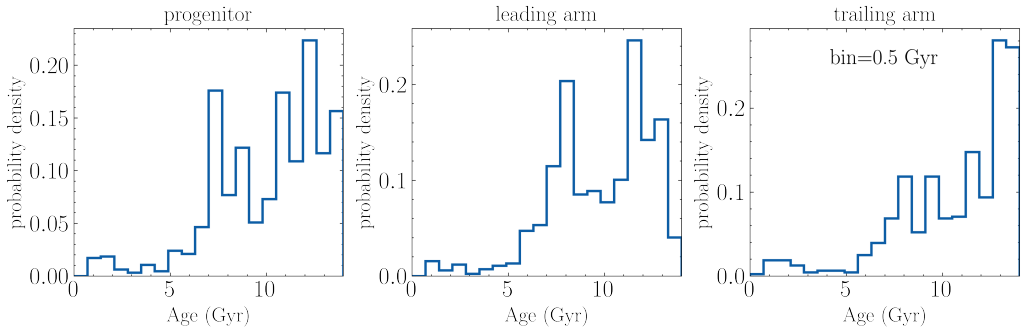

Figure 3.8: *Normalized probability distribution function of the age for the progenitor (left), the leading arm (middle), and the trailing arm (right) of the Sgr satellite.*

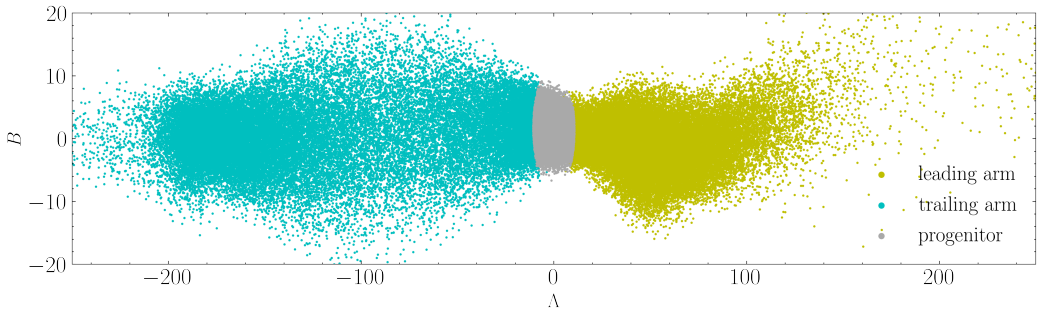

Figure 3.9: *The Sgr simulation particles in the right-handed celestial coordinate. The bound particles which represent the progenitor of the Sgr are illustrated by grey points. The leading and trailing arms are shown in yellow and cyan colors.*

two arms. They find that the interaction of Sgr with the MW potential led the gas to strip away, truncating the star formation about $\approx 5-7$ Gyr ago. The leading arm has a SFH, which peaks at 7 and 11 Gyr, whereas the trailing arm has a relatively older population and peaks at 9 Gyr ago. We adopt an average SFH for the progenitor of the Sgr. We assign ages to Sgr simulation particles such that they reconstruct the estimated age distributions shown in Figure 3.8.

Similar to the Galactic halos, we use the Sgr simulation particles as the progenitors for the DWDs, and then randomly draw a number of binaries from the synthetic population according to Equation (3.2). The masses and positions from the Sgr simulation are passed down to the sample, as are the ages from the estimated SFH. The DWDs are then evolved to their assigned ages. Again, binaries with SNR > 7 are identified as potential GW sources in LISA detections.

Chapter 4

Results

4.1 Galactic halo

Based on a combination of the cosmological simulation and the DWD binary population synthesis model, we obtain the population of detectable binaries in a MW-like Galactic halo. We demonstrate how DWDs can be used to constrain the global properties of satellites and streams within the Galactic halo.

The first four columns in Table 4.1 show the properties of the simulated Galactic halos. Only about 1.5 percent of the binary systems in this population have formed and not merged yet, with frequencies that fall within the LISA sensitivity range. In the simulations, the Z direction is set up to be perpendicular to the plane of the Galactic disk. We adopt three equally distant points on the $x-y$ plane for the Sun location, assuming it is located at a distance of $R_{\odot} = 8.1$ kpc from the Galaxy center (Abuter et al., 2018). We calculate the number of binary systems within each halo that can be individually resolved for mission durations of 4 and 10 years considering a duty cycle of 75% and 100% averaged on three solar viewpoints. As we would expected, the number of resolved binaries increases as the observation time gets longer. We observe that the most massive halo, halo07, with a relatively large distance from the galactic center, halo contains 1066 detectable DWDs. On the other hand, a halo with an intermediate-mass, halo 09, contains almost the same number of detectable DWDs because of its relatively small distance. According to our findings, the most massive and youngest halo, halo 07, with a relatively large median distance from the Galactic center, includes the most detectable DWDs. Also, halo 09 with an intermediate mass contains almost the same number of observable binary systems because of its significantly lower median distance. As

expected, halo 08 has the fewest detected binaries with a smaller mass, a large distance, and a relatively old population.

In Figure 4.1, we observe the surface density of the resolved binary systems in halo 02, with an edge on and face on view. Assuming that the Sun is located at (8.1, 0, 0) kpc, we observe that, with the exception of the density peak in the Galactic center, the number of detectable DWDs decreases with increasing distance from the Sun.

Figure 4.2 shows the characteristic strain and frequency of the DWDs within halo 02 in the LISA sensitivity range. We see that almost all of the DWDs with $f > 2$ mHz have a SNR> 1, regardless of distance, and may therefore be resolved. It is worth noting that we used a SNR threshold of 7 for detectability.

As an example, we describe the population of DWDs and those that are detectable in satellite 37 of halo 02. Since we considered a constant density of 0.039 DWD$/M_{\odot}$, we expect that the DWD population traces the stars' density. The satellite with a mass comparable to that of Sgr, an old population ($>$ 9 Gyr), and a median distance of 30 kpc, includes 22 resolved binaries in a single populating run.

We would like to now investigate the global characteristics of satellites such as mass, age, and distance within the simulated halos via their detectability in LISA. Combining the detectable satellites, which contains more than two resolved binaries, we see no clear correlation between the number of the detected binaries and the satellites' median age and median distance, as shown in Figure 4.4. However, we see a weak correlation between the number of resolved binaries and the total mass of the satellites. Ignoring the outliers which lose detectability due to their large median distances, we can fit a power law relation $N_{det} = 6.55 \times 10^{-9} M_{\star}^{1.16}$ to it.

Figure 4.5 shows the histogram of the total stellar mass, the median age, and the median distance of the satellites and those that contain more than two detectable binary systems from all of the simulated Galactic halos combined. The detection efficiency in each bin is defined as the ratio of detected satellites to all satellites in that bin. As a result, satellites with masses greater than $10^8 M_{\odot}$ are most likely visible in LISA. We may also conclude that a satellite must have a minimum mass of $5 \times 10^6 M_{\odot}$ in order to host LISA detections. The Galactic halos contain a relatively old population of stars. Therefore, they lack a dominating population of CO-CO tracers and do not provide us with useful data for satellites with stellar populations younger than 10 Gyr.. At older ages $>$ 10 Gyr, we can nearly observe that the satellite's detectability is independent of its age. We see that the satellites are typically positioned approximately 30 kpc from the center of the Galaxy. At lower distances, detection efficiency correlates

Version of August 18, 2021– Created August 18, 2021 - 10:17

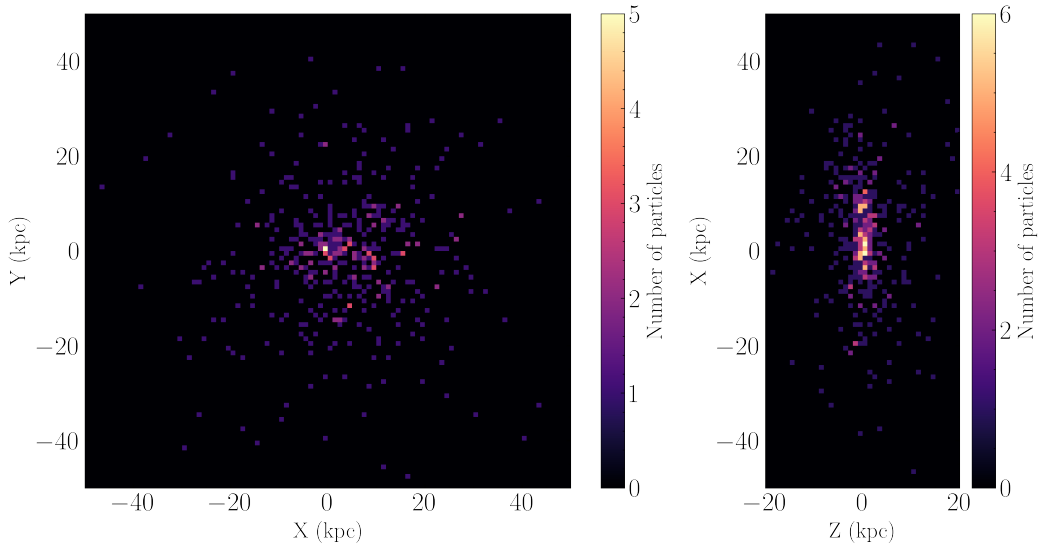

Figure 4.1: *Density map of the detectable binary sources in the simulated Galactic halo 02, viewed faced on (left) and edge-on (right).*

with the distance, and over 30 kpc, satellites' abundance and detectability decline.

In Figure 4.6, we observe the median distance and the total stellar mass of the satellites, as well as the number of observable binaries indicated by their color. More massive satellites, in general, have more detectable binaries. At each mass bin, we see that the satellites contain less detectable binary systems at higher distances. The massive satellites located in the upper right of Figure 4.6 do not have many observable binaries due to their far distances.

We may now describe the contribution of different subtypes of DWDs to the population of resolved binaries by LISA. Table 4.2 indicates that He-He and He-CO DWDs are over-represented in the population of resolved binaries compared to the binary population synthesis model (assuming a burst star formation). Because the formation time for He-He DWDs is comparatively longer and due to the old population of Galactic halo stars, this subtype dominates the population of resolved binaries. On the other hand, CO-CO and ONe-X DWDs generated from recent star formations have already merged and are under-represented.

Halo ID	M_{tot} ($\times 10^9$ $M_\odot$)	D (kpc)	τ (Gyr)	$N_{DWD,LISA}$ ($\times 10^6$)	Resolved with LISA 4yr		10yr	
					75%	100%	75%	100%
02	5.37	30.9	11.5	3.23	853	989	1322	1482
05	3.53	21.3	12.3	2.05	810	909	1185	1327
07	6.91	39.1	11.3	4.29	1066	1244	1668	1900
08	3.21	28.8	12.4	1.97	291	351	489	574
09	4.63	16.3	11.9	2.73	1046	1203	1568	1763
10	3.58	29.0	12.3	2.17	465	540	733	835
12	5.65	25.9	11.9	3.47	480	557	770	889
14	3.84	25.6	12.6	2.34	515	588	791	910
15	2.88	28.7	15.6	1.76	353	416	563	651
17	3.53	25.9	12.5	2.15	426	510	721	848
20	2.86	26.8	12.4	1.66	444	508	690	782
Avg	4.18	27.1	12.4	2.53	613	710	954	1087

Table 4.1: *Summary of the properties of the simulated Galactic halos, as well as the number of sources individually resolved by LISA over time. From left to right, we mention the Halo ID, which shows the halo number in the Galactic halo simulations given by Bullock & Johnston (2005), the total mass (M_{tot}), the median distance (kpc), and the median age of the halos. Then the number of DWDs that are in the LISA frequency range is presented for each halo. The four columns on the right indicate the number of resolved binary systems for 4 and 10 years of observation with 75% and 100% duty cycles.*

Halo ID	CO-CO	He-CO	He-He	ONe
02	5.5%	24.2%	69.8%	0.5%
05	5.5%	23.8%	69.7%	1.0%
07	6.7%	21.2%	71.5%	0.6%
08	5.1%	25.1%	69.4%	0.4%
09	4.1%	21.7%	73.5%	0.7%
10	8.1%	23.2%	67.7%	1.0%
12	7.2%	26.8%	65.2%	0.8%
14	7.7%	21.6%	70.5%	0.2%
15	8.3%	24.4%	66.8%	0.5%
17	6.9%	26.5%	66.1%	0.5%
20	7.0%	24.0%	68.1%	0.9%
Avg	6.6%	23.9%	68.9%	0.6%

Table 4.2: *Summary of the contribution of DWDs with different core compositions to the detectable binaries in each simulated Galactic halo.*

Version of August 18, 2021– Created August 18, 2021 - 10:17

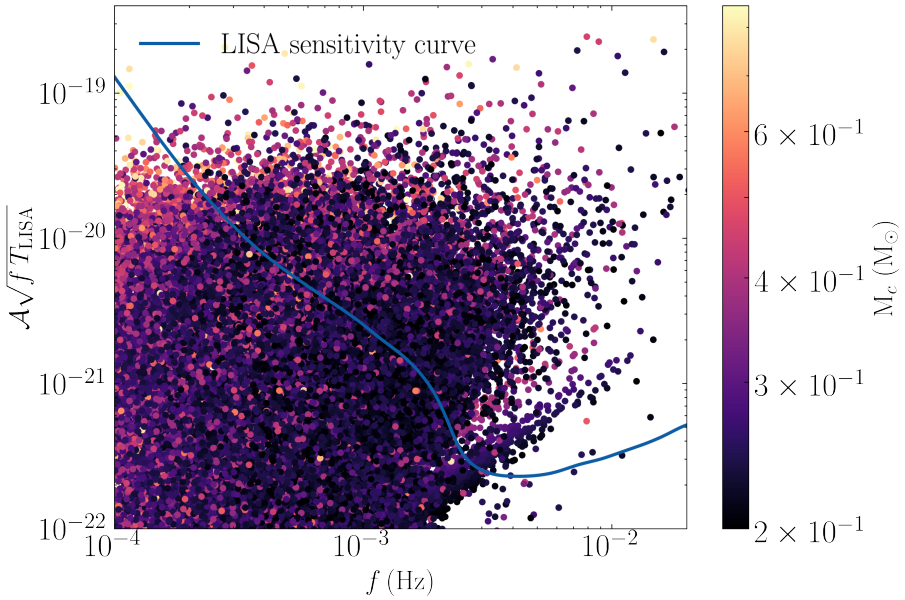

Figure 4.2: *Characteristic strain and frequency of the population of DWDs in the simulated halo 02. The color bar represents the chirp mass of the DWDs. The solid line indicates the Sensitivity curve of LISA.*

4.2 Sagittarius

Combining the binary population synthesis model with the Sgr simulation and using the observed SFH, we may calculate the number of its detected binaries. Random selection of binaries from the synthetic population causes one result to differ slightly from another. To eliminate this random error, we run the populating code ten times and average the results. Table 4.3 shows the summary of the number of resulted binaries in the progenitor, the leading arm, and the trailing arm of the Sgr. The progenitor is the most massive component of the Sgr and hosts around 20 binaries with 4 years of observation and a 75% duty cycle. The leading and trailing arms have almost similar masses and contain the same number ≈ 5 of detected binaries. The simulated Sgr has a mass of $2 \times 10^8 M_\odot$ and contains an average of around 30 detected DWDs. The fitted equation from the analysis of the simulated halo, shown in Figure 4.4, predicts 31 observed binaries, which is consistent with this result.

Figure 4.7 shows the Gaussian kernel density estimated from the resolved binaries of the Sgr satellite. We show that observable binaries are most likely found in streams near the Sgr's progenitor, which correlates to a higher mass density. Therefore, the likelihood of finding streams distant

Version of August 18, 2021– Created August 18, 2021 - 10:17

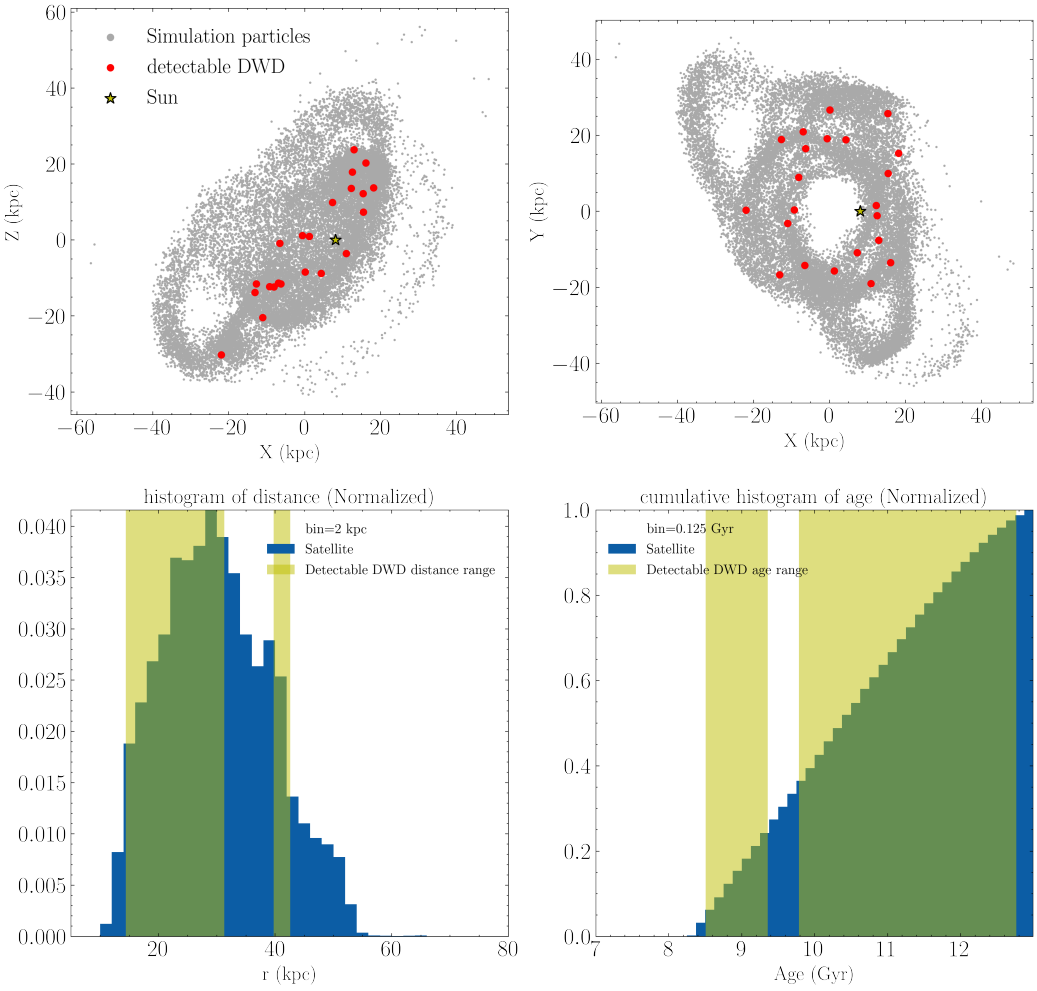

Figure 4.3: *Description of the population of DWDs in satellite 37 of halo 02. Top panels demonstrate the population of DWDs (grey points) and those that can be detected (red points) within this satellite on the $x-y$ and $x-z$ planes. The yellow star indicates the position of the sun. The normalized histogram of distance (bottom left) and the cumulative distribution of the satellite's age (bottom right) are shown. The detected binaries have an age and a distance within the range of the yellow patches.*

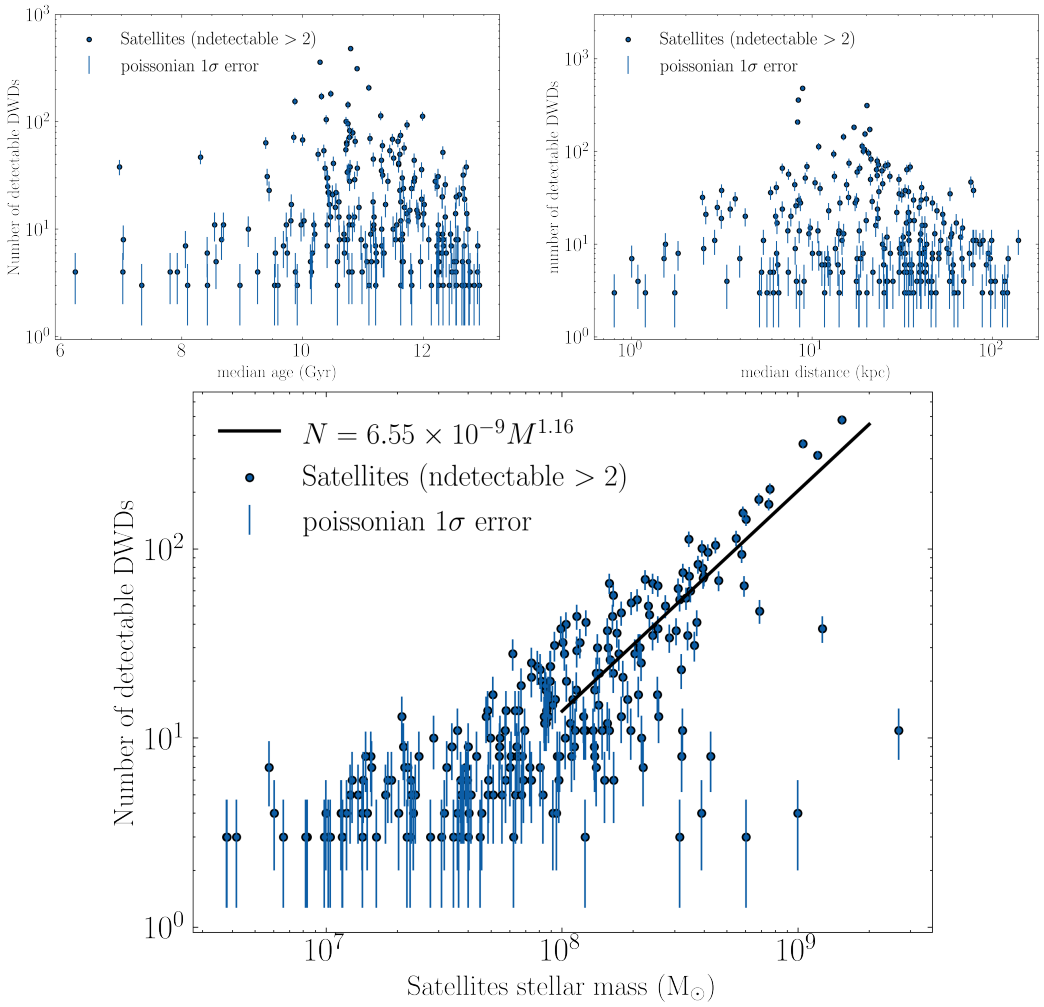

Figure 4.4: *The number of resolved binary systems as a function of the median age (top left), the median distance (top right), and the total stellar mass (bottom) of the satellites from all simulated halos combined. In these figures, each point indicates a satellite that contains more than two detectable binaries. We include a power law fit to satellites with masses more than $10^8 M_\odot$, while disregarding satellites with large masses and extremely large median distances.*

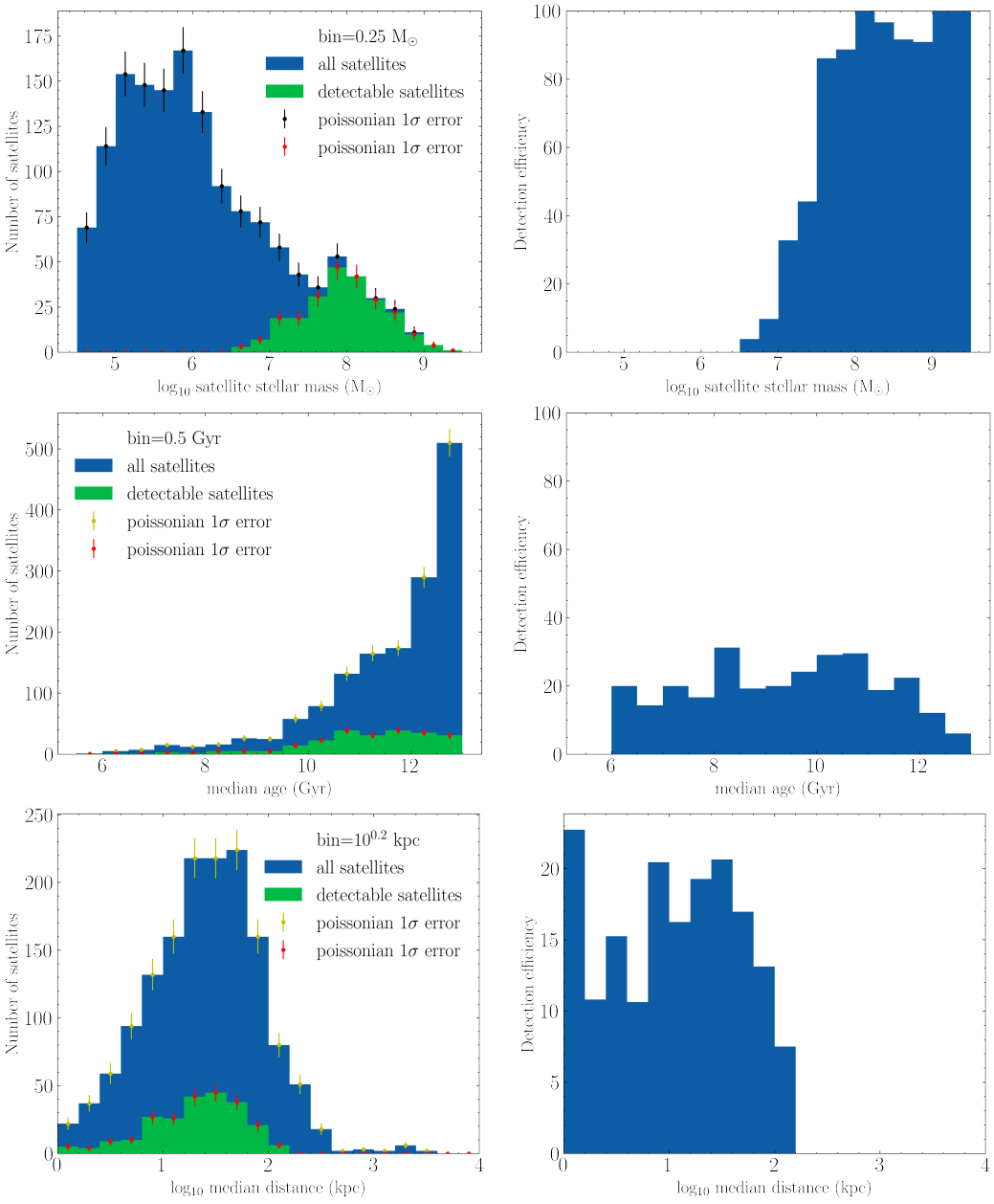

Figure 4.5: *Histogram of the total mass (top left), the median age (middle left), and the median distance (bottom left) of all satellites (in blue) and those that contain more than two detectable binaries (in green). The right panels indicate the ratio of detected satellites to total satellites in each bin.*

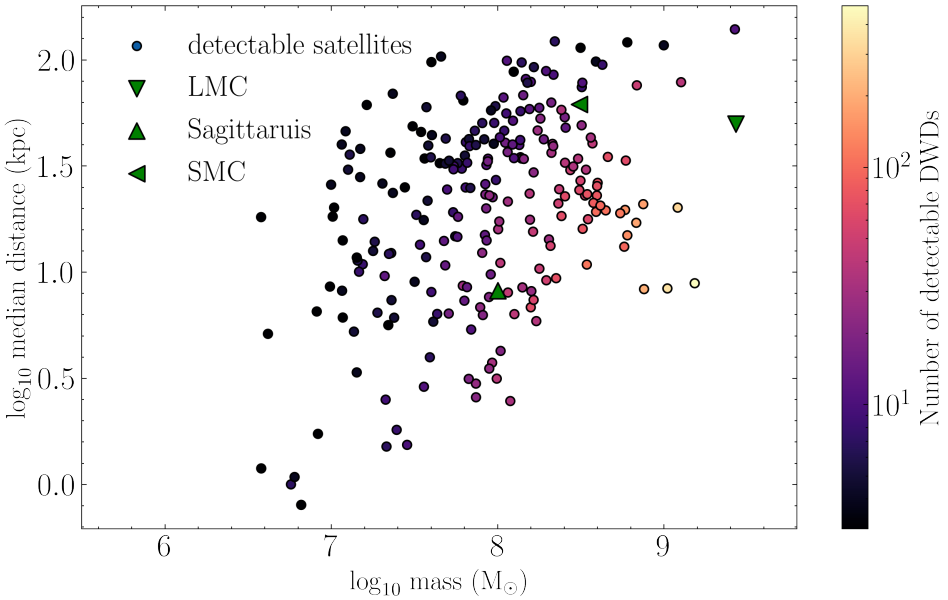

Figure 4.6: *The median distance as a function of the total mass of the satellites from the simulated Galactic halos. The number of resolved binaries within each satellite is indicated by the color bar. Green triangles represent some of the known satellites: LMC, SMC, and Sgr.*

from the progenitor is low. In Table 4.4 we can see the core composition of the detectable binaries in the Sgr components. We adopted an old age distribution with a median age of > 10 Gyr, which resulted in the resolved binary systems having a dominant He-He type population. We can also observe that the leading arm with younger population of stars contains more CO-CO types of DWDs than the trailing arm.

	M_{tot} ($\times 10^6$ $M_\odot$)	$N_{DWD,LISA}$ ($\times 10^3$)	Resolved with LISA 4yr 75%	4yr 100%	10yr 75%	10yr 100%
Progenitor	111	38.4	19.5±3.1	22.0±3.5	34.2±5.4	40.5±5.7
Leading arm	45	15.8	4.8±1.6	5.9±1.6	8.9±2.5	10.3±2.9
Trailing arm	43	14.4	5.1±2.9	6.6±3.2	8.6±4.4	10.2±4.1

Table 4.3: *Summary of the number of sources resolved by LISA in the Sgr satellite, averaged over ten runs. From left to right, we list the total mass of each component of Sgr, the number of DWDs within the LISA frequency range, and the number of resolved binaries considering mission duration of 4 and 10 years with 75% and 100% duty cycles.*

	CO-CO	He-CO	He-He	ONe
Progenitor	6.7%	37.9%	52.3%	3.1%
Leading arm	18.8%	35.4%	45.8%	0.0%
Trailing arm	7.8%	21.6%	64.7%	5.9%
Avg	8.8%	34.7%	53.4%	3.1%

Table 4.4: *Summary of the core composition of resolved sources by LISA in the Sgr satellite.*

Version of August 18, 2021– Created August 18, 2021 - 10:17

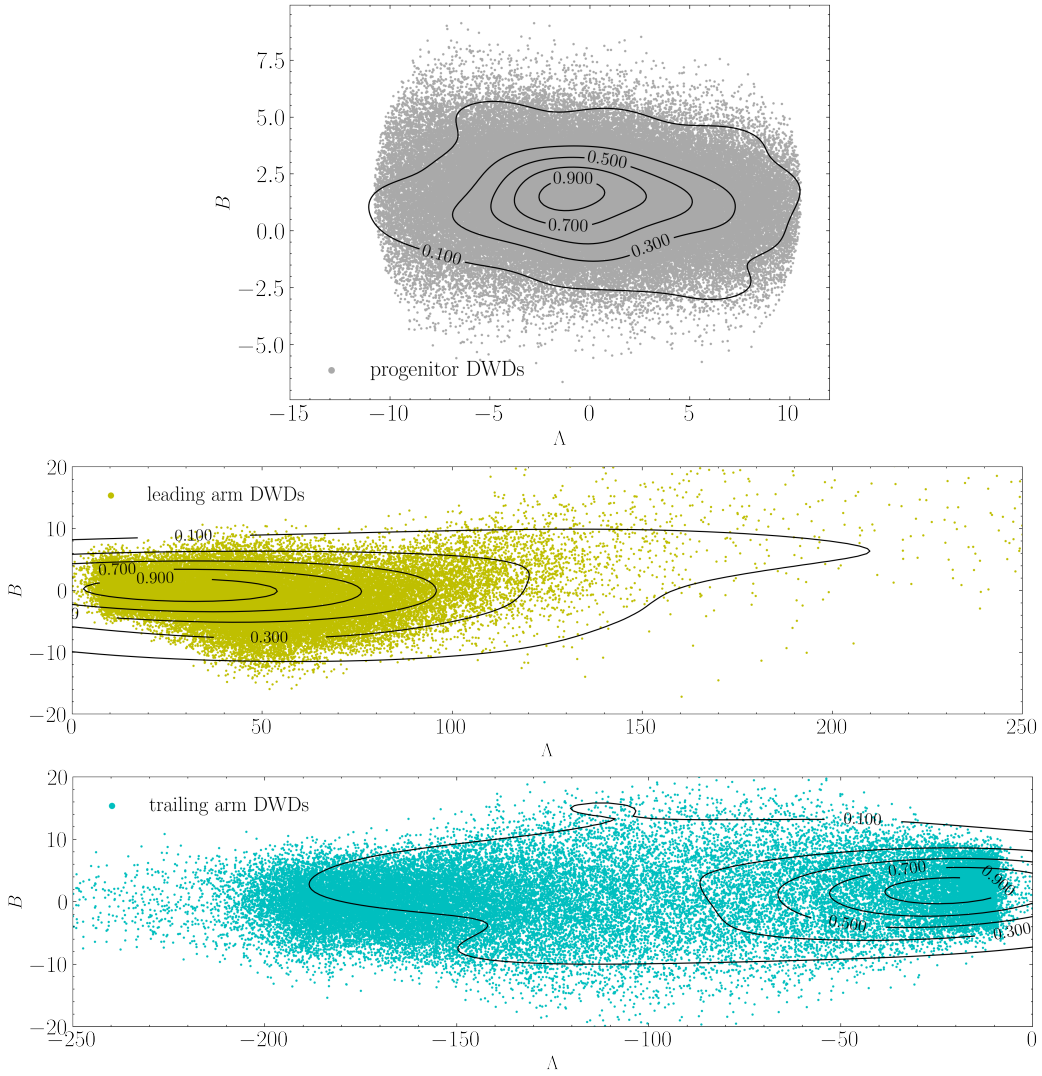

Figure 4.7: *Contours on the celestial coordinate system representing the Gaussian kernel density estimated from detectable binaries with levels at 10%, 30%, 50%, 70%, and 90% of the peak density for the progenitor (top), the leading arm (middle), and the trailing arm (bottom) of the Sgr.*

Chapter 5

Discussion and Conclusion

We have constructed a DWD population model for the Galactic halo combining a binary population synthesis model and a simulation of MW like halo. Eleven Galactic halo models are taken from a cosmological simulation by Bullock & Johnston (2005), which consistently reproduced the observed characteristics. We then determined how binaries can be detected by LISA. We studied the global properties of these halos, and their satellites and streams by their detected binaries. According to their mass and distance distributions, they contribute differently to the GW signals.

We estimated $\sim$ 200 million binaries in each halo, of which over $\sim$ 2.5 million are within the LISA frequency range, and about 600 will be individually resolved throughout the nominal four-year course of mission with a 75% duty cycle. We demonstrated that all binaries with $f > 2$ mHz have a SNR> 1, thus may be potential sources for LISA, consistent with Lamberts et al. (2019). Our binary evolution model predicts that 6% of the detected systems are CO-CO, 24% CO-He, 69% He-He, and less than 1% ONe-X. Since the Galactic halo has an old stellar population, the fraction of He-He systems, which have a relatively long formation time, increases over time. On the contrary, CO-CO and ONe-X binaries, which trace the young population of stars, are under-represented. By studying the substructures of the Galactic halos, we showed that the most important parameter affecting a satellite detectability in GWs is the total stellar mass. At the same time, larger distances may significantly reduce the number of detected binaries. We found an empirical relation between the number of LISA detections and the total stellar mass for the satellites.

In comparison, Ruiter et al. (2009) used the similar technique of employing a binary population synthesis model to investigate the contribution of halo DWDs to LISA signals. They obtain 27.5×10^6 DWDs, which

is an overestimation based on our results and is most likely due to the lower frequency sensitivity of 0.01 mHz they adopt for LISA. They find that He-He systems dominate in the Galactic halo, which is supported by our findings. Roebber et al. (2020) demonstrated in a similar study that the MW satellites with a stellar mass of $10^6 M_\odot$ host enough binaries to be detected by LISA. We confirm this conclusion requiring the satellites to have a factor of 5 larger stellar mass to host LISA detectable binaries. The bulge, thin and thick disk, and the halo of MW are extensively studied by Korol et al. (2020), and Lamberts et al. (2019) employing binary population synthesis models. They predicted that the Galactic halo and its substructures contain LISA detections. Our work produces a similar number of detectable sources and complements their efforts by looking further into the MW satellites and streams.

In this work, we showed that GW astronomy can be used to probe the MW halo. We provided one of the first studies looking into the MW satellites and stellar streams in GWs. We demonstrated that LISA detections could help us to constrain the stellar mass of the MW satellite and streams. Moreover, we showed that LISA could detect known MW satellites and streams and potentially discover new ones with masses of $> 5 \times 10^6 M_\odot$ through populations undetected in the EM observations.

We provide the first model of the population of DWDs in the Sgr satellite and streams by combining the binary population synthesis model with a Sgr simulation and using a SFH determined by photometric and spectroscopic observations. The Sgr model is constructed by an N-body simulation of the tidal disruption of a spherical progenitor on the MW + LMC potential. We study the Sgr potential LISA resolved binaries.

We estimated $\sim$ 8 million binaries in the Sgr, of which over $\sim$ 65 thousands are within the LISA frequency range. About 30 will be individually resolved throughout the nominal four-year course of mission with a 75% duty cycle. Our binary evolution model predicts that 9% of the detected systems are CO-CO, 35% CO-He, 53% He-He, and fewer than 3% ONe-X. Since we adopted an old age for the population of stars in the Sgr, He-He types dominate in the observable binaries similar to the Galactic halo. Inside the Sgr, the leading arm hosts more CO-CO DWDs as of its younger age compared to the trailing arm.

5.1 Limitations

Our research is based on a cosmological simulation of the Galactic halo showing consistency with the observed characteristics of the MW halo and

Version of August 18, 2021– Created August 18, 2021 - 10:17

its satellite. However, the eleven simulated halos vary in global properties. None reconstruct the MW halo perfectly, and they all lack the equivalent of the LMC, which hosts a large number of LISA sources. The main uncertainty in these simulations is caused by employing a smoothly growing potential, which prevents them from predicting any major or minor merger with good accuracy. Another drawback is that the interactions between satellites are not tracked.

The binary population synthesis model we used is consistent with the observations. However, it is highly dependent on the assumptions for the binary and stellar evolution parameters, affecting the mass distributions, formation time, and the orbital separation of the binaries. More specifically, the main uncertainty stems from the common envelope phase treatments. However, the current and the future EM surveys, such as Gaia, Vera Rubin Observatory and possibly E-ELT, will supply us with a large number of DWD statistics, reducing the uncertainties in our synthetic population models.

In the study of the Sgr, we used an N-body simulation data calibrated by the observations. This model also inevitably contains several uncertainties rising from their assumptions. The most notable is that the Sgr has a spherical, non-rotating progenitor that prevents reproducing the observed bifurcation in the stream. In addition, the leading arm shows a 2° offset comparing to the observed track.

5.2 Further research

The measurements of several observable parameters, such as the chirp mass, which is computed by the measurement of the frequency derivative, benefit from a longer observation time. Furthermore, accuracy of the measurement of sky localization is enhanced by a longer mission duration, which can be employed to extract the EM counterparts from wide-field surveys such as Gaia and E-ELT. LISA can give us an independent distance measurement that can be combined with the posterior probability distribution derived from parallax measurements by Gaia to enhance the distance estimations. Our method provides a DWD population of the Galactic halo that may be used to improve LISA data analysis, particularly to compute the background confusion noise caused by the unresolved binaries.

Version of August 18, 2021– Created August 18, 2021 - 10:17

Acknowledgements

Financial support was provided in the form of a scholarship from the Den Adel Fund.

Version of August 18, 2021– Created August 18, 2021 - 10:17

Bibliography

Abbott B. P., et al., 2016a, Phys. Rev. D, 93, 112004

Abbott B. P., et al., 2016b, , 116, 061102

Abbott B. P., et al., 2017, Phys. Rev. Lett., 119, 161101

Abt H. A., 1983, , 21, 343

Abuter R., et al., 2018, Astron. Astrophys., 615, L15

Amaro-Seoane P., et al., 2013, GW Notes, 6, 4

Amaro-Seoane P., et al., 2017a

Amaro-Seoane P., et al., 2017b, arXiv e-prints, p. arXiv:1702.00786

Belokurov V., et al., 2014, , 437, 116

Benacquista M., Holley-Bockelmann K., 2006, , 645, 589

Broek D. v. d., Nelemans G., Dan M., Rosswog S., 2012, Mon. Not. Roy. Astron. Soc., 425, 24

Bullock J. S., Johnston K. V., 2005, , 635, 931

Cornish N., Robson T., 2017, J. Phys. Conf. Ser., 840, 012024

Cseresnjes P., Alard C., Guibert J., 2000, , 357, 871

Dehnen W., Odenkirchen M., Grebel E. K., Rix H.-W., 2004, , 127, 2753

Duchêne G., Kraus A., 2013, , 51, 269

Duffau S., Zinn R., Vivas A. K., Carraro G., Méndez R. A., Winnick R., Gallart C., 2006, , 636, L97

Eggleton P. P., 1983, , 268, 368

Einstein A., 1915, Sitzungsberichte der Königlich Preußischen Akademie der Wissenschaften (Berlin, pp 844–847

Einstein A., 1916, Sitzungsberichte der Königlich Preußischen Akademie der Wissenschaften (Berlin, pp 688–696

Einstein A., Rosen N., 1937, Journal of The Franklin Institute, 223, 43

Evans C. R., Iben Icko J., Smarr L., 1987, , 323, 129

Folkner W. M., Bender P. L., Stebbins R. T., 1998, in American Astronomical Society Meeting Abstracts #192. p. 17.08

Gibbons S. L. J., Belokurov V., Evans N. W., 2017, Mon. Not. Roy. Astron. Soc., 464, 794

Glampedakis K., Kennefick D., 2002, Phys. Rev. D, 66, 044002

Hamanowicz A., et al., 2016, , 66, 197

Heggie D. C., 1975, , 173, 729

Helmi A., 2020, , 58, 205

Hils D., Bender P. L., Webbink R. F., 1990, , 360, 75

Hughes S. A., 2006, AIP Conf. Proc., 873, 13

Hulse R. A., Taylor J. H., 1975, , 195, L51

Ibata R. A., Gilmore G., Irwin M. J., 1994, Nature, 370, 194

Ibata R. A., Lewis G. F., Irwin M. J., 2002, Mon. Not. Roy. Astron. Soc., 332, 915

Ibata R., et al., 2021, , 914, 123

Jiang I.-G., Binney J., 2000, , 314, 468

Johnston K. V., 2016, Origins and Interpretation of Tidal Debris. p. 141, doi:10.1007/978-3-319-19336-6_6

Johnston K. V., Zhao H., Spergel D. N., Hernquist L., 1999, Astrophys. J. Lett., 512, L109

King I., 1962, , 67, 471

Koposov S. E., et al., 2018, , 479, 5343

Korol V., Rossi E. M., Groot P. J., Nelemans G., Toonen S., Brown A. G. A., 2017, , 470, 1894

Korol V., Koop O., Rossi E. M., 2018, , 866, L20

Korol V., Rossi E. M., Barausse E., 2019, Mon. Not. Roy. Astron. Soc., 483, 5518

Korol V., et al., 2020, Astron. Astrophys., 638, A153

Kroupa P., 2001, Mon. Not. Roy. Astron. Soc., 322, 231

Lacey C., Cole S., 1993, , 262, 627

Lamberts A., Blunt S., Littenberg T. B., Garrison-Kimmel S., Kupfer T., Sanderson R. E., 2019, , 490, 5888

Larson S. L., Hiscock W. A., Hellings R. W., 2000, Phys. Rev. D, 62, 062001

Lau M. Y. M., Mandel I., Vigna-Gómez A., Neijssel C. J., Stevenson S., Sesana A., 2020, Mon. Not. Roy. Astron. Soc., 492, 3061

Law D. R., Majewski S. R., 2010, , 714, 229

Maggiore M., 2007, Gravitational Waves. Vol. 1: Theory and Experiments. Oxford Master Series in Physics, Oxford University Press

Majewski S. R., Skrutskie M. F., Weinberg M. D., Ostheimer J. C., 2003, Astrophys. J., 599, 1082

Malhan K., Ibata R. A., 2018, , 477, 4063

Marsh T. R., Nelemans G., Steeghs D., 2004, Mon. Not. Roy. Astron. Soc., 350, 113

McKenzie K., Spero R. E., Shaddock D. A., 2009, Phys. Rev. D, 80, 102003

Moore B., Ghigna S., Governato F., Lake G., Quinn T. R., Stadel J., Tozzi P., 1999, Astrophys. J. Lett., 524, L19

Navarro J. F., Frenk C. S., White S. D. M., 1996, , 462, 563

Nelemans G., Yungelson L. R., Portegies Zwart S. F., Verbunt F., 2001a, Astron. Astrophys., 365, 491

Nelemans G., Yungelson L. R., Portegies Zwart S. F., 2001b, Astron. Astrophys., 375, 890

Newton O., Cautun M., Jenkins A., Frenk C. S., Helly J. C., 2018, , 479, 2853

Portegies Zwart S. F., Verbunt F., 1996, , 309, 179

Purcell C. W., Bullock J. S., Kazantzidis S., 2010, , 404, 1711

Robson T., Cornish N. J., Liu C., 2019, Class. Quant. Grav., 36, 105011

Roebber E., et al., 2020, The Astrophysical Journal, 894, L15

Ruiter A. J., Belczynski K., Benacquista M., Holley-Bockelmann K., 2009, , 693, 383

Ruiter A. J., Belczynski K., Benacquista M., Larson S. L., Williams G., 2010, , 717, 1006

Sesana A., Lamberts A., Petiteau A., 2020, Mon. Not. Roy. Astron. Soc., 494, L75

Tong D., 2019, Lectures on General Relativity.

Toonen S., Nelemans G., Portegies Zwart S., 2012, , 546, A70

Toonen S., Hollands M., Gänsicke B. T., Boekholt T., 2017, , 602, A16

Vasiliev E., Belokurov V., 2020, , 497, 4162

Vasiliev E., Belokurov V., Erkal D., 2021, , 501, 2279

Weinberg S., 1972, Gravitation and Cosmology: Principles and Applications of the General Theory of Relativity

Zolotov A., Willman B., Brooks A. M., Governato F., Brook C. B., Hogg D. W., Quinn T., Stinson G., 2009, , 702, 1058

Zorotovic M., et al., 2011, , 536, L3

de Boer T. J. L., Belokurov V., Koposov S., 2015, , 451, 3489